Research Square

Preprints are preliminary reports that have not undergone peer review.
They should not be considered conclusive, used to inform clinical practice,
or referenced by the media as validated information.

The senescence-linked factor Chi3L1 contributes to mesenchymal stromal cells dysfunction promoting joint aging and osteoarthritis progression

Georges Maroun
Institute for Regenerative Medicine & Biotherapy
Anne-Laure Bonnefont
Institute for Regenerative Medicine & Biotherapy
Raissa Silva
Université de Montpellier
Claudia Terreza
Institute for Regenerative Medicine & Biotherapy
Carolina Pradenas
Institute for Regenerative Medicine & Biotherapy
Catalina Asencio
Institute for Regenerative Medicine & Biotherapy
Bruno Robert
Institut de Recherche en Cancérologie de Montpellier
Dominique De Seny
Centre Hospitalier Universitaire de Montpellier
Frédéric De CEUNINCK
Institut Servier
Philippe Pastoureau
Institut Servier
Christian Jorgensen
Institute for Regenerative Medicine & Biotherapy
Farida Djouad
Institute for Regenerative Medicine & Biotherapy
Yves-Marie Pers
Institute for Regenerative Medicine & Biotherapy
Jean-Marc Brondello
jean-marc.brondello@inserm.fr

Institute for Regenerative Medicine & Biotherapy

Article

Keywords:

Posted Date: October 29th, 2026

DOI: https://doi.org/10.21203/rs.3.rs-11363315/v1

License: This work is licensed under a Creative Commons Attribution 4.0 International License.
Read Full License

Additional Declarations: No competing interests reported.

Abstract

Ageing progressively disrupts joint homeostasis and increases susceptibility to osteoarthritis (OA), yet why repair fails in the altered joint remains poorly understood. Cellular senescence accumulates with age and is prominent in osteoarthritic joints, contributing to a persistent catabolic, inflammatory and tissue-remodelling microenvironment through the senescence-associated secretory phenotype (SASP). Such signals can alter the function of endogenous reparative cells including mesenchymal stromal cells (MSCs), which are important to tissue repair and immunomodulation. Nonetheless, little is known on which senescence associated stromal factors within this altered niche could compromise MSCs competence. In this study, we are interested by chitinase-3-like 1 (CHI3L1), a SASP glycoprotein whose levels are elevated in both ageing and OA. We revealed that CHI3L1 accumulates in OA joints in correlation with senescence and the disease features, where it in vitro chronic exposure converts MSC toward a dysfunctional age-like state characterized by impaired potencies, disrupted tri-lineage commitment, reduced mobility, altered metabolomic profiling, loss of immunomodulatory activity together with an acquisition of a pro-inflammatory secretome. Consequently, CHI3L1 preconditioning abolishes the homeostatic function of healthy MSCs in an inflammatory OA model. Conversely, in spontaneous age-related OA model, MSC transplantation combined to CHI3L1 transient neutralization restores joint dynamics by enhancing cartilage repair, reducing synovial inflammation, preventing bone remodeling, improving maximal speed locomotor and shifting selective circulated factors related to stromal, skeletal, and hematopoietic homeostasis toward a more youthful pattern. Collectively, our findings establish CHI3L1 as a novel senescence-associated contributor in the decline of MSC fitness and regenerative niche competence during joint ageing. Furthermore, it provides a rationale for combining microenvironment-targeted interventions with stem cell therapy to maximize their potentials for tissue regeneration in age-related diseases.

Introduction

Osteoarthritis (OA) is the most prevalent degenerative joint disorder affecting over 600 million individuals worldwide with approximately 73% of whom are aged above 55 years[1]. Long viewed as a degenerative cartilage disease, OA is now recognized as an age-driven disorder of whole-joint tissue homeostasis failure. Cartilage erosion, synovial inflammation, subchondral bone remodeling, osteophyte formation, and chronic pain collectively reflect the inability of aging joint tissues to preserve structural integrity and effective regenerative responses. Understanding the mechanisms underlying this age-related loss of joint homeostasis which ultimately drives OA onset has become a central challenge in regenerative medicine[2].

Joint homeostasis is in part maintained by tissue-resident mesenchymal stromal cells (MSCs), a heterogeneous population of cells reside in the synovium, subchondral bone, cartilage, and surrounding connective tissues[3]. Beyond their multilineage differentiation potential, MSCs continuously sense mechanical, inflammatory, and metabolic cues from their microenvironment to promote tissue repair[4,5]. Through self-renewal, trophic support, extracellular matrix remodeling, and immunomodulatory signaling,

they are believed to maintain tissue integrity and orchestrate communication among stromal, immune, and skeletal cells[6–8] .These properties have made MSCs an attractive therapeutic candidate for OA over the past decades[9–13]. However, MSC-based therapies have produced inconsistent clinical benefits[11–13], particularly in elderly patients with OA, suggesting that the aged joint microenvironment progressively loses its permissiveness to respond to regenerative signals and ultimately to restore homeostasis[14].

Accordingly, accumulating evidence indicates that ageing profoundly remodels stem cell niches across multiple organs including joint, resulting in progressive loss of resident stem cell fitness to maintain tissue homeostasis rather than simple depletion of stem cell numbers[15–18]. One of the principal drivers of niche ageing is cellular senescence[19,20]. In response to tissue injuries during lifespan such as mechanical overload, inflammation, oxidative stress, or metabolic dysfunction, joint cells including MSC undergo durable cell-cycle arrest while acquiring extensive metabolic and secretory remodeling known as the senescence-associated secretory phenotype (SASP)[21–24]. Whereas transient senescence contributes to development, wound healing, and tissue remodeling[25–27], persistent senescent cells especially within the joint establish a chronic pro-inflammatory and matrix-remodeling environment that disrupts tissue homeostasis [28–30]. Consistently, pharmacological or genetic clearance of senescent cells attenuates OA progression and restores a more regenerative joint environment in preclinical models, highlighting the pivotal role of senescence in loss of joint homeostasis and OA pathogenesis [31–39]. Importantly, the detrimental effects of senescence indeed extend beyond direct tissue degeneration to include disruption of the endogenous regenerative compartment[40–42]. For instance, the exposure of healthy human MSCs to pro-senescent OA synovial fluid impairs their clonogenicity, differentiation, immunomodulatory activity and therapeutic efficacy[43] while senescent bone marrow-derived MSCs (BM-MSCs) accelerate cartilage degeneration and subchondral bone alterations in vivo[44,45]. Together, these observations support the emerging concept that chronic exposure to age-driven senescence-associated signals progressively compromises MSC fitness and functions ultimately exhausting the regenerative niche leading to OA. However, the soluble mediators responsible for this microenvironment-driven loss of joint homeostasis remain largely unknown.

Chi3L1 (also known as YKL-40 in humans and BRP-39 in mice) has emerged as a compelling candidate. Chi3L1 is a secreted chitinase-like glycoprotein whose circulating levels increase with ageing[46,47] and are consistently associated with chronic inflammatory, fibrotic, and degenerative diseases[48–52]. In OA, Chi3L1 is widely used as a biomarker of disease severity detected in synovial fluid and systemic circulation.[53–55] Nevertheless, whether Chi3L1 actively contributes to regenerative dysfunction or simply reflects ongoing joint damage remains unresolved. Given its established roles in extracellular matrix remodeling, immune regulation, and tissue remodeling[51,56–58], we hypothesized that persistent high level of Chi3L1 may act as a senescence-associated niche signal which progressively remodels resident MSC function and limits the regenerative capacity of the ageing joint. Here, we demonstrate that Chi3L1 accumulates within OA-driven senescent joints in both human and murine models. Chronic exposure to Chi3L1 impairs the fitness of healthy young BM-MSCs, ultimately driving the acquisition of a

dysfunctional age-associated phenotype characterized by diminished regenerative potential. Importantly, Chi3L1 neutralization restores aged regenerative niche competency by markedly enhancing MSCs-mediated repair in spontaneous age-related murine OA model. Collectively, our findings establish Chi3L1 as an active regulator of regenerative niche exhaustion rather than simply a biomarker of OA and provide a rationale for combining niche-targeted interventions with stem cell therapy to promote tissue regeneration in age-related diseases.

Results

Induced expression of the stromal factor CHI3L1 tracks joint senescence and OA disease severity across mice and humans

In our recent publications, we demonstrated that senescent cells are present among the three joint compartments namely, cartilage, subchondral bone and synovial tissue in both clinical and preclinical samples[44,59]. Strikingly, using the ganglioside GD3, a novel senescence cell-surface marker and the expression of its synthase namely *ST8SIA1*, we identified a subpopulation of senescent fibroblast-like synoviocytes that also expresses *CHI3L1*[59] in OA tissues. To confirm these findings, we re-analyzed publicly available single-cell RNA sequencing datasets from OA synovium. Among nine different synovial-associated cell type populations identified by UMAP analysis, we confirmed that *CHI3L1* expression was predominantly detected within *THY1*$^{+}$, *ST8SIA1*$^{+}$, *CXCL12*$^{+}$ senescent inflammatory fibroblast-like synoviocytes sub-population (Fig. 1A and S1). Gene expression analysis of independent OA synovial specimens further demonstrated a positive correlation (r = 0.9286, P = 0.0067) between *CHI3L1* and the senescence marker *CDKN2A* confirming the relationship between joint senescence and *CHI3L1*-associated OA pathogenesis (Fig. 1B-C).

To investigate whether CHI3L1 is also found associated with senescence markers in joint and synovium of experimental OA model, we then examined its expression in collagenase-induced OA (CiOA) murine model. Forty days after intraarticular collagenase injection, mice developed the pathological features, including cartilage degeneration, synovitis, and subchondral bone remodeling evaluated by associated histological scoring and microCT analysis (Fig. 1D-J), confirming successful establishment of the disease. We then assessed Chi3L1 expression. OA mice exhibited a marked increase in circulating CHI3L1 protein compared with control mice (Fig. 1K). Likewise, whole-joint gene expression analysis revealed significant upregulation of *Chi3L1* together with canonical senescence hallmarks, including *Cdkn2a* and *Cdkn1a*, and representative SASP-associated genes (Fig. 1L). Chi3L1 expression, positively correlated with senescence markers *Cdkn2a (r = 0.7173, P = 0.0240)* and *Cdkn1a (*r = 0.6909, P = 0.0226), indicating that its induction accompanies activation of the senescence program during OA (Fig. 1M). We next focused on Chi3L1 level in synovial tissue. Chi3L1 expression was significantly increased in synovial from OA joints and positively correlated with *Cdkn1a*, (r = 0.7129, P < 0.0001) *Cdkn1c* (r = 0.6621, P < 0.0001) *Mmp13*, (r = 0.8690, P < 0.0001) and *Tgfb1* (r = 0.7873, P < 0.0001) (Fig. 1N-R), demonstrating that Chi3L1 expression is closely associated with local senescence and tissue-remodeling programs. Finally, we examined the relationship between *CHI3L1* expression and disease stage in the CiOA model.

Both synovial *Chi3L1* expression and plasmatic Chi3L1 concentrations positively correlated with OA severity ($r = 0.6984$, $P < 0.0001$ and $r = 0.6909$, $P = 0.0226$ respectively) (Fig. 1S-T) confirming previous observations made in human studies[42,60,61]. Together, these findings identify CHI3L1 as a senescence-associated stromal factor whose expression increases during OA and disease severity across mice and humans. These observations prompted us to determine whether targeting senescent cells *in vivo* could mitigate joint degeneration while reducing CHI3L1 expression in OA mice.

Pharmacological suppression of senescence reduces CHI3L1 expression in vitro and during experimental OA

To confirm that CHI3L1 is a component of the SASP, we first examined the *in vitro* effect of the well-characterized senomorphic agent metformin on its production by senescent cells[39,62]. Senescence was induced in mouse embryonic fibroblasts (MEFs) by etoposide treatment, followed by incubation with metformin or vehicle as described (Fig. 2A). Seven days post-treatment, we showed that etoposide induced a robust senescent phenotype characterized by an inhibition in cell proliferation and an increased senescence-associated β-galactosidase activity, which was significantly attenuated by metformin treatment (Fig. 2B-C). Consistent with CHI3L1 being a SASP component, senescent MEFs secreted significantly higher levels of CHI3L1 than proliferating cells, whereas metformin treatment markedly reduced its secretion (Fig. 2D). We next investigated whether the observed *in vitro* metformin senomorphic effect, similarly regulates Chi3L1 expression while attenuating OA progression *in vivo*. Metformin administration was initiated ten days after collagenase-induced OA and maintained throughout disease progression (Fig. 2E). At euthanasia, joint histological analysis revealed that metformin treatment significantly attenuated cartilage degeneration compared with vehicle-treated controls (Fig. 2F-G), confirming the reported chondroprotective effects of metformin in mice and OA patients[63–65]. Importantly, this structural improvement was accompanied by a marked reduction in circulating Chi3L1 concentrations (Fig. 2H). Whole-joint gene expression analysis further demonstrated decreased expression of *Chi3L1* together with canonical senescence markers and representative SASP-associated genes following metformin treatment (Fig. 2I). Similar effects were observed within the synovium, where metformin reduced synovitis severity (Fig. 2J-K) and concomitantly downregulated *Chi3L1, Cdkn1a, Cdkn1c, and Tgfb1* expression (Fig. 2L). In contrast, metformin did not significantly restore subchondral bone structure altered in CiOA joints (Supp Fig. 2). Together, these findings demonstrate that pharmacological suppression of senescence by Metformin attenuates OA progression while reducing CHI3L1 expression both *in vitro* and *in vivo*. Taken together, these data position CHI3L1 as a senescence-linked factor and implicate sustained CHI3L1 in OA pathogenesis.

Chronic exposure to CHI3L1 compromises mesenchymal stromal cell fitness and promotes an age-associated senescence-like phenotype

Our previous comparative proteomic analysis of DNA damage induced senescent bone marrow-derived MSCs (BM-MSC) identified CHI3L1 as one of the most strongly upregulated secreted factors compared with mock treated MSCs[44]. To determine whether this association extended to chronological ageing, we re-analyzing a publicly available transcriptomic dataset comparing BM-MSCs from donors aged to 21 to 92 years together with MSCs undergoing replicative senescence[66]. Remarkably, *CHI3L1* was identified within a core gene signature shared by both chronologically aged and replicative senescent MSCs (Fig. 3A). Consistent with these observations, CHI3L1 expression and secretion were similarly increased in two independent MSC induced senescence models generated by silencing *FERMT2* or *CBX4*, two genes whose expression declines in MSC during ageing and OA[67–69] (Supp Fig. 3A-F). Together, these data position CHI3L1 at the intersection of MSC senescence and chronological ageing that characterize OA patients. We next asked whether CHI3L1 could be part of the senescence-driven microenvironment that alters the regenerative niche within the aged joint and thereby drives OA progression. To address this question, we *in vitro* assessed the tissue repair properties of healthy young BM-MSCs following continuous exposure to recombinant CHI3L1 at a physio-pathological concentration (100 ng/mL), comparable to levels reported in the synovial liquid and the circulation of OA patients[70] (Fig. 3B).

Chronic CHI3L1 treatment markedly reduced MSC clonogenic potential in an IL13RA2 dependent manner, (Fig. 3C-D) consistent with IL13RA2 serving as a major receptor for CHI3L1[56]. Reduction in CFU occurred without an increase in apoptotic cell death (data not shown). In parallel, CHI3L1 constrained BM-MSCs population expansion, with increased population doubling time and reduced proliferation (Fig. 3E). Therefore, we next asked whether this decline was accompanied by acquisition of a senescence-like phenotype. CHI3L1-treated MSCs displayed increased senescence-associated β-galactosidase activity together with induction of *ARF*, *CDKN1A* and *CDKN2A* gene expression and a slide increase in $p16^{INK4a}$ protein abundance (Fig. 3G-H).

Because joint homeostasis relies on both efficient MSC recruitment at the injured site and their multipotent capacities to differentiate, we then evaluated these two critical regenerative functions. Chronic CHI3L1 exposure significantly impaired CXCL12-directed migration of MSC in trans-well assay, recapitulating a key feature of age-associated MSC dysfunction (Fig. 3I-J). Furthermore, CHI3L1 profoundly altered MSC lineage commitment, reducing both chondrogenic and osteogenic differentiation while promoting adipogenesis as revealed by dedicated staining (Fig. 3K-T). These MSC functional changes were respectively accompanied by increased expression of the catabolic marker *MMP13* during chondrogenesis, reduced *ALP* expression during osteogenesis, and enhanced *PPARG2* expression during adipogenesis, thus consistent with the known impaired skeletal tissue regeneration with aging[71–73].

Given the critical role of metabolites in stem-cell functions, we asked whether the observed CHI3L1-induced MSC dysfunction could be explained by alterations in their metabolic status. Untargeted metabolomic profiling of treated MSC from 3 donors compared to untreated cells respectively revealed marked changes in metabolites involved in redox homeostasis, including a reduction in NAD+, changes in glutathione (GSH/GSSG) ratio, and γ-glutamyl-cysteine, together with alterations in metabolites

associated with extracellular matrix synthesis and lineage specification such as proline, hydroxyproline, and uracil (Fig. 3U). Collectively, all these changes closely resemble signatures reported in aged MSCs[74,75] and might explain the broad impact of CHI3L1 treatment on MSC properties. In conclusion, chronic CHI3L1 exposure drives premature loss of MSC fitness and acquisition of an aging-like phenotype.

Chronic exposure to CHI3L1 reprograms the immunoregulatory properties of mesenchymal stromal cells

In our previous untargeted metabolomic profiling, CHI3L1-treated MSCs displayed a distinct metabolic signature including 4-aminobutyric acid (GABA), citrulline, and arginosuccinate (Fig. 3T) known to regulate MSC immunoregulatory properties (Fig. 4A)[76], The decreased abundance in these metabolites proposed a shift of the CHI3L1-treated MSC toward a pro-inflammatory and immunologically dysfunctional phenotype[77,78]. Accordingly, treated MSC showed a pronounced positive switch in IFN-γ, MCP1, IP-10, IL-6, IL-4 and IL-12p70 release (Fig. 4B) compared to untreated cells. These changes suggested a shift away from their anti-inflammatory homeostatic state that supports MSC immunomodulatory functions[79]. Because MSC-mediated immune regulation also relies on juxtacrine mechanism, we next analyzed by flow-cytometry the expression of the immune checkpoint PD-L1 and PD-L2 that have emerged as players of MSC-mediated immunoregulatory activity[80–82]. CHI3L1-pretreated MSCs displayed significantly reduced surface expression of both molecules (Fig. 4C-F), compared to non-treated MSCs suggesting a loss in their immunosuppressive properties.

We next confirmed that all these phenotypic changes translated into immunological functional consequences. For that, untreated or CHI3L1-pretreated MSCs were co-cultured with activated peripheral blood mononuclear cells (PBMCs) from healthy donors as described (Fig. 4G). Whereas untreated MSCs efficiently suppressed PBMC proliferation, CHI3L1-preconditioned MSCs exhibited a markedly reduced immunosuppressive capacity (Fig. 4H). Impaired MSC-mediated immunosuppression was observed on both activated $CD4^+$ and $CD8^+$ T-cell populations (Fig. 4I) and was associated with increased frequencies of IFNγ-producing $CD4^+$ T cells and T-bet^+/$IFN\gamma^+$ $CD8^+$ effector T cells (Fig. 4J-K), indicating enhanced inflammatory T-cell activation. Consistent with this impaired immunoregulatory phenotype, conditioned media from CHI3L1-treated MSC-PBMC co-cultures contained significantly lower concentrations of bioactive TGF-β1 than control co-cultures (Fig. 4L), indicating reduced activation of one of the major immunosuppressive pathways employed by MSCs[83,84].

Collectively, these data demonstrate that CHI3L1 chronic exposure alters MSCs properties, eroding their stemness multipotency and immunosuppressive properties. Together these observations support a model in which joint senescence occurring during age-related OA establishes a CHI3L1-dependent feed-forward stromal signaling axis that reinforces local inflammaging and loss of regenerative fitness within the niche (Fig. 4M).

CHI3L1-conditioned mesenchymal stromal cells lose their capacity to preserve joint homeostasis in vivo

Having established that persistent CHI3L1 *in vitro* reprograms MSCs toward an age-like, functionally impaired state, we next asked whether these alterations compromise their joint homeostaticproperties *in vivo*. To address this question, murine BM-MSCs were first chronically exposed to recombinant murine CHI3L1 under the same conditions used for human MSCs (Fig. 5A). Consistent with our previous findings, CHI3L1 treatment reduced murine MSC proliferation and impaired their immunosuppressive activity toward activated splenocytes (Fig. 5B-C), demonstrating that CHI3L1-induced functional reprogramming is conserved across species. We then determined the joint homeostaticproperties of these CHI3L1-conditioned MSCs in two-month-old CiOA mice, in which articular delivery of untreated MSCs are known to be effective by projecting joint from degeneration[85–87]. CHI3L1-preconditioned murine MSCs were injected intra-articularly ten days after OA induction in parallel to untreated MSCs. Joint pathology was assessed seven weeks later (Fig. 5D). As previously published by us and others, transplantation of untreated MSCs significantly limited cartilage degeneration in this experimental OA model confirming their repair and anti-inflammatory properties [86,88–90] (Fig. 5E-F). In striking contrast, CHI3L1-conditioned MSCs failed to confer such cartilage protection with histological OA scores comparable to mock treated joints (Fig. 5E-F). Loss of protective potencies of these injected cells was accompanied by broad molecular alterations within the joint. Indeed, whereas untreated MSCs reduced the expression of senescence-associated genes altogether with inflammatory and catabolic mediators, CHI3L1-conditioned MSCs largely failed to normalize these pathways and exhibited persistent or enhanced expression of matrix-remodeling and fibrotic genes, including *Mmp13* and *Tgfb1* (Fig. 5G). Similarly, untreated MSCs markedly attenuated synovitis score, whereas CHI3L1-conditioned MSCs showed no detectable anti-inflammatory effects (Fig. 5H). Within the subchondral bone compartment, untreated MSCs also displayed a protective trend by limiting bone erosion and preserving trabecular architecture, particularly in the lateral compartment. Notably, the beneficial effects of injected MSC were abolished in CHI3L1-treated MSC groups (Fig. 5I-N) consistent with the impaired differentiation potential of human CHI3L1-treated MSCs observed *in vitro* (Fig. 3).

Collectively, these data demonstrate that chronic CHI3L1 exposure is sufficient to induce regenerative dysfunction in mesenchymal stromal cells *in vivo*. MSC pre-exposed to CHI3L1 lost their ability to limit cartilage degeneration, synovitis and pathological joint remodeling. In contrast, untreated MSCs retained significant protective efficacy following their intra-articular delivery despite transient exposure to the CHI3L1-enriched joint microenvironment. These results identify sustained CHI3L1 conditioning, rather than short-term local exposure, as a critical determinant of MSC dysfunction.

Combined CHI3L1 neutralization and MSC delivery restores articular homeostasis in aged-driven osteoarthritic joints

Our findings support the concept that persistent high level of CHI3L1 found in old individuals may participate to OA progression by functionally disabling resident MSC homeostatic competence. We therefore hypothesized that inhibiting CHI3L1 with a neutralizing monoclonal antibody would promote a resetting of the stem cell niche microenvironment in old individuals. We relied on the previously published[91] neutralizing anti-murine CHI3L1 antibody, to test whether CHI3L1 blockage alone or combined with functional MSC delivery could prevent senescence and delay age-induced joint degeneration. Seventeen-month-old mice received intraperitoneal injections of anti-CHI3L1 antibody or isotype control (5 mg/kg) every three days, followed by a single intra-articular injection of BM-MSC or vehicle and a final intraperitoneal injection of anti-CHI3L1 antibody, according to the experimental design shown in Fig. 6A. Forty days after the last injection, full joint analysis on sacrificed mice revealed that neither CHI3L1 neutralization nor MSC administration alone substantially delayed age-driven joint degeneration. In marked contrast, combined therapy produced the most pronounced therapeutic benefit with a significant decrease in senescence gene expression particularly *Cdkn2a* in the whole joint (Fig. 6B) and accordingly, a significant reduction in cartilage degeneration compared with all other groups (Fig. 6C-D). In parallel, a significant reduced synovitis score evaluated by histology was reported in synovial tissue (Fig. 6E). We therefore profiled the synovial transcriptome to determine the molecular changes that associated with this resolution of synovial inflammation. As shown on Fig. 6F, combination therapy induced the largest transcriptional remodeling, with 644 differentially expressed genes relative to aged controls, whereas antibody or MSC monotherapy produced only modest changes (Fig. 6F). Pathway enrichment analysis demonstrated coordinated down regulation of inflammatory, innate immune, extracellular matrix, oxidative stress, and metabolic pathways (Fig. 6G). Consistent with this extensive remodeling, genes implicated in matrix turnover, inflammatory signaling, and stromal activation including *Chi3L1, Ccn2, Cxcl12, Cxcr4, Il1b, Adam8, Mtor, Fos, Tnfsf10*, *S100a9, Sod3, Fabp4, Adipoq* were selectively normalized following combination therapy (Fig. 6H) In addition, improvements in osteoarticular bone structure were also observed predominantly in the combined treatment group compared to untreated aged mice (Fig. 6I-L). Indeed, microCT analyses revealed increase in bone volume, density, connectivity and preservation of trabecular organization further supporting restoration of joint homeostasis (Fig. 6I-N). Importantly these local skeletal changes were accompanied by improved maximal running speed despite no significant change in total distance traveled displayed, in open-field test (Fig. 6R-S).

Based on these foundations, we next investigated whether these effects on local joint tissue repair were also associated with a rejuvenation of the mesenchymal stromal cell communication network within the whole organism. Blood samples analysis by Nulisa of treated groups confirmed that combination therapy shifted the circulating proteomic profile toward that observed in young healthy animals (Fig. 6T). These included an increase in (Cellular Communication Network factor 4 (CCN4), a matricellular protein that promotes stem-cell regenerative capacity[92] but also Wnt family member 16 (WNT16), a critical regulator of osteoblast-osteoclast coupling whose decline contributes to cortical porosity[93], osteoclast activation[94], and impaired osteogenic differentiation of MSCs during aging.[94,95] Furthermore, we found an increase in Glycoprotein Non-Metastatic Melanoma Protein B (GPNMB), a stromal factor that

supports MSC immunomodulation, bone maintenance, and tissue repair[96–98] altogether with an increase in Fms-like tyrosine kinase 3 ligand (FLT3LG) and Kit Ligand/ Stem cell factor (KITLG), two essential stromal regulators of hematopoietic stem-cell survival, maintenance, migration, immune regeneration, and bone marrow niche resilience/integrity[99–104].

Collectively, our results demonstrate that CHI3L1 neutralization is sufficient to create a permissive niche in which transplanted MSCs recover their regenerative potential to restore tissue homeostasis in aged OA joints. CHI3L1 acts as a senescence-induced negative regulator of the stromal niche that progressively erodes MSC fitness thus limiting endogenous tissue repair and facilitating age-related OA degeneration.

Discussion

Adult tissue homeostasis depends on continuous communication between resident stem cells within their niche and their microenvironment[105]. Aging progressively remodels this niche, reducing stem-cell fitness and regenerative capacity, while the accumulation of senescent stem cells amplifies these changes through persistent secretion of senescence-associated factors. Within the osteoarthritic aged joint, senescence features have been found in different articular cell types and especially mesenchymal stromal cells.[31,37,40–42,59,106] How senescence and its associated SASP factor reshapes joint regenerative niche remains poorly understood. Here, we identify CHI3L1 as a senescence-regulated stromal signal that links senescence to regenerative failure. Chronic CHI3L1 exposure induced a coordinated loss of MSC fitness characterized by reduced clonogenicity, impaired migration, altered lineage commitment, metabolic remodeling and limited immunoregulatory activity. These alterations closely resemble hallmarks of aged MSCs[74,75], suggesting that high level of circulating CHI3L1 found in old individuals, does not simply induce local functional defects but could drive a stable transition toward an age-associated stromal identity across tissue.

Previous studies have associated CHI3L1 with numerous age-related diseases including OA severity and fibrosis[107–110], whereas others have reported protective functions during acute tissue damage[111,112]. For instance, our observed data contrast with the recent study showing that CHI3L1 overexpression attenuates experimental OA by suppressing TLR4-MAPK-STAT1 inflammatory signaling in chondrocytes[113]. However, our findings reconcile these seemingly divergent observations by supporting a context-dependent model. Similar to cellular senescence itself and other SASP components[114], transient CHI3L1 induction may support tissue adaptation and repair following injury, whereas its persistent accumulation in the aged and pro-senescent microenvironment becomes maladaptive by chronically remodeling the stromal niche. CHI3L1 may also shape the immune and skeletal microenvironment by regulating CD4 + T-cell polarization[115] but also neutrophil recruitment[116] and osteoclast mediated bone-resorption [117,118], ultimately further compromising endogenous joint repair with ageing. In this setting, CHI3L1 emerges not merely as a biomarker of OA in old individuals but as a senescence-regulated mediator that progressively reprograms both the functional identity of resident

mesenchymal stromal cells and the joint immune landscape. Consistent with this model, systemic CHI3L1 neutralization combined with MSC therapy restored a regenerative microenvironment of the aged joint. This combinatorial strategy preserved cartilage architecture, improved subchondral and trabecular bone integrity, and increased bone connectivity, indicating coordinated restoration of joint homeostasis. Beyond these structural improvements, combined treatment profoundly remodeled the inflammatory and immune landscape of the aged synovium while simultaneously shifting the circulating plasmatic profile of treated mice toward a more youthful state. Importantly, the regulated factors from stromal origin converged on biological pathways governing regeneration and tissue homeostasis. For instance, CCN4, GPNMB, and KITLG are all established regulators of stem-cell maintenance and regenerative niche function[119–121], whereas WNT16 is a critical determinant of osteoblast-osteoclast coupling and bone integrity whose decline contributes to skeletal aging.[93] Likewise, restoration of FLT3LG, a key regulator of hematopoietic progenitor maintenance and immune regeneration[100,122,123], further supports the notion that CHI3L1 blockade remodels not only the local joint environment but also the systemic effects on MSC-driven regenerative and osteoimmune networks.

Although our findings identify CHI3L1 as a key regulator of the regenerative stromal niche within the joint, the signaling pathways mediating these effects remain to be fully defined. Previous studies identified IL13RA2 as a principal CHI3L1 receptor and also reported its increased expression in aged MSCs[124], raising the possibility that aging enhances cellular responsiveness to CHI3L1. Together with evidence that CHI3L1 activates ERK, AKT and NF-κB signaling[56,125,126], our data support a feed-forward model in which age-induced senescence both increases CHI3L1 production and sensitizes stromal cells to its signaling that lock the tissue in an established deleterious stressing inflammatory loop progressively reinforcing regenerative failure. Future studies using conditional genetic models targeting CHI3L1 or IL13RA2 will be important to define the contribution of this axis to tissue aging and repair.

Finally, one of the most important implications of our study is that successful regenerative therapy for elderly people requires correction of both the regenerative cells and their surrounding microenvironment. MSC therapy alone was insufficient to overcome the inhibitory effects of the aged niche, whereas CHI3L1 neutralization alone incompletely restored osteo-articular homeostasis. Only the combined strategy effectively remodeled senescence and inflammatory pathways, reduced structural joint damage, improved bone architecture and locomotor activities while restoring circulating youthful factors. These findings support the emerging concept that regenerative medicine applied to old individuals should restore both stem cells and their niche rather than either component alone to treat age-related degenerative diseases.

Materials and methods

Cell types collection and culture conditions

Human MSC collection were purchased from Hannover Medical School after obtaining written informed consent and approval from the local and national ethics committees (votum N°.2562) as previously published[44]. Bone marrow aspirates of young, age- and sex-matched healthy donors (mean age 30 ± 10 years, n = 4) were cultured and amplified to select MSC in complete alpha-minimum essential medium supplemented with 10% fetal bovine serum (FBS), 1% penicillin/streptomycin, 2 mM L-glutamine at 37°C, 5%CO2. For the upcoming experiment and methods all the BM-MSCs were use at early passage (between p3-p4). For Mouse Embryonic fibroblast, MEF were provided by Dr. Daujat at IRMB-CHU-Montpellier. They were isolated from embryonic tissue of Swiss mice from pregnant females at embryonic day 14 then maintained as adherent fibroblasts in culture. Once thawed MEFs were cultured in complete Dulbecco's Modified Eagle Medium (DMEM) supplemented with 10% heat-inactivated fetal bovine serum (FBS), 1% penicillin/streptomycin, 2mM L-glutamine at 37°C, 5%CO2, for two days. MEF were then seeded at 20k cell/cm^2 density into T25 culture flasks. Once the cells reached 90% confluency, they were ready to be splitted into p2 and used for following treatment and later experiments. For murine BM-MSCs isolation, 4weeks old C57 Bl6JNJ right leg. Femur and tibia were dissected, and diaphysis were flushed with PBS. Cell suspensions were filtered and plated at a concentration of $1x10^6$ cells/cm^2 in DMEM medium supplemented with 10% FBS (Hyclone, Thermo Fisher Scientific), 2mM glutamine, 100U/mL penicillin, 100mg/mL streptomycin (Lonza, Levallois-Perret, France) and 2ng/mL human basic fibroblast growth factor (R&D Systems, Lille, France). Medium was changed daily to remove red blood cells and non-adherent cells. BM-MSCs were stored at -80°C after passage 1.

For senescence induction, two different methods have been applied. First one, senescence induction on MEF, cells were seeded at 5000cell/cm^2 for 24h then treated with 20 µM of Etoposide (Sigma E1383) or the vehicle control DMSO overnight. 3 experimental conditions were assessed: (i) Treated with DMSO (proliferative condition) (ii) Treated with etoposide (senescent condition) (iii) treated with etoposide then supplemented with metformin (senescent + metformin condition. In the following day medium was replaced and metformin was freshly dissolved to 3mM and added to the corresponding condition. Cells were maintained in culture for a week with medium changes every three days. Senescence levels were evaluated after seven days: SN has been collected and cells were fixed for SA-ß-gal staining. The second one, BM-MSCs were transfected with scramble siRNA control or siFERMT2 or siCBX4 respectively according to RNimax protocol transfection and cultivated for ten days. Senescence levels were evaluated by SA-B-gal staining, cell counting, RTqPCR and Elisa.

For Chi3L1 treatment, rhChi3L1 (Biotechne #2599-ch-050) or rmChi3L1 (Biotechne #2649-ch-50) was dissolved in PBS to a 100ng/mL. BM-MSCs were seeded at 2000cells/cm^2 density. One day after seeding, cells were treated with recombinant Chi3L1 at 100ng/mL for fourteen days, while parallel untreated BM-MSCs received PBS only. Two weeks later, cells were collected and subjected to various analyses, depending on the specific experiment.

Colony Forming Unit (CFU) assays

For CFU assays, according to the ISCT recommendations: $1x10^3$ MSCs were homogeneously seeded in 60mm dishes. rhChi3L1 (100ng/ml) has been chronically each two to three days. while parallel untreated BM-MSCs received PBS only. Ten days later, once cell colonies emerged, cultures were fixed with methanol 80% and stained with Giemsa (Merck # 32884) dye solution diluted 1:20 for counting.

IL13RA2 RNA ablation and CFU effect

To evaluate the effect of siIL13A2 transfection effect on CFU formation, BM-MSCs were seeded $5x10^3$ cells/cm^2 in a 6 well plates. Once the cells attained 70% confluency, they were transfected twice at day 0 and day 2 with siCtrl or the siRNA targeting IL13Rα2 (Santa Cruz, USA) at 50nM using Oligofectamine™ (Thermo Fisher Scientific #12252011) according to the manufacturer's instructions. The following days, cells were collected seeded in 60mm dishes and CFU protocol was conducted as previously. Four experimental conditions were established: (i) siCtrl-transfected MSC untreated and, (ii) siCtrl-transfected MSC treated with rhChi3L1 100ng/ml, (iii) siIL13RA2-transfected MSC untreated (PBS as vehicle control) (iiii) siIL13RA2-transfected MSC treated with rhChi3L1 100ng/ml. Analyses has been assessed as previously described.

Proliferation and Population DoublingTime (PDT) calculation

For proliferation assay, BM-MSCs were seeded at 2000cells/cm^2 density. One day after seeding, cells were treated with rhChi3L1 at 100ng/mL for fourteen days, while parallel untreated BM-MSCs received PBS only. Cells were harvested and counted using a Countess™ 5 Automated Cell Counter (Thermo Fisher Scientific) following the manufacturer's instructions. Viability was assessed using trypan blue exclusion. Following seeding for the proliferation assay, the PDT was determined through culture in each passage using the formula PD = T/LOG2n with T= culture time and n=cell number fold increase during culture periode.

Senescence-associated β-galactosidase activity

Induction of MSC senescence was assessed by staining MSCs with a senescence-associated β-galactosidase (SA-β-Gal) Staining Kit (Sigma-Aldrich #CS0030) according to the manufacturer's instructions. $12x10^3$ BM-MSCs were plated in 12-well plates overnight following the end the treatment period. The next day, cells were fixed at RT for 8min with the kit's fixation solution, and then overnight incubated with the SA-β-Gal staining solution to reveal SA-β-Gal activity. Cells displaying blue cytosolique staining were classified as positive. Images of random fields for each sample were acquired by microscopy to cover the entire well, and at least 300 cells were counted per sample. Positive cells were quantified, normalized to the total cell count, and expressed as a percentage.

Chi3L1 secretome analysis

For senescent human BM-MSCs (Etoposide and siRNA), Chi3L1 in cell supernatant were quantififed by Elisa (R&D biotechne, Human Chitinase 3-like 1/YKL-40 DuoSet ELISA #DY2599). Procedure was performed according to the manifacturer's instructions, and steps were repeated as described previously for mouse serum samples, with exception: samples were diluted at 1:10 in dilution buffer prior incubation. For senescent MEF and metformin supplementation, Chi3L1 in cell supernatant were quantififed by Elisa (R&D biotechne, Mouse Chitinase 3-like 1/YKL-40 DuoSet ELISA #DY2649). Proedsure was performed according to the manifacturer's instructions, and steps were repeated as described previously for mouse serum samples, with exception: samples were diluted at 1:1 in dilution buffer prior incubation.

In vitro mesenchymal stromal cell differentiation

The trilineage differentiation potential of human BM-MSCs was evaluated using commercial chondrogenic (Stemcell Technologies, #05455), adipogenic (#05412), and osteogenic (#05465) differentiation media according to the manufacturer's instructions.

For chondrogenic differentiation BM-MSC ($5x10^5$ cells) were cultured as micropellets and maintained for 21 days. Two experimental conditions were established: (i) micropellet of BM-MSC cultured in complete Chondrogenic Differentiation Medium (differentiated condition), (ii) micropellet of BM-MSC cultured in complete Chondrogenic Differentiation Medium in the presence of rhChi3L1 (100ng/ml) (differentiated Chi3L1-treated condition). For all conditions, the medium was replaced every three days, maintaining the corresponding treatment or vehicle control. Cartilage matrix formation was assessed by Safranin O/Fast Green staining and quantified using ImageJ. Chondrogenic differentiation was further evaluated by RT-qPCR analysis of *COL2A1*, *COL10A1*, and *MMP1*.

For osteogenic differentiation BM-MSC were seeded at $2x10^4$ cells/cm^2 were seeded, cultured until reaching 90% of confluency then differentiated. Three experimental conditions were established: (i) BM-MSCs maintained with complete αMEM (proliferative condition) (ii) BM-MSC cultured in complete Osteogenic Differentiation Medium (differentiated condition), (iii) BM-MSC cultured in complete Osteogenic Differentiation Medium in the presence of Chi3L1 (100ng/ml). For all conditions, the medium was replaced every three days, maintaining the corresponding treatment or vehicle control. At the end of differentiation period, matrix mineralization Matrix mineralization was quantified by 2% Alizarin Red S staining (562 nm), and osteogenic differentiation was assessed by RT-qPCR for *ALP*, *SPP1* and *BGLAP*.

For adipogenic differentiation, BM-MSC were seeded at $6x10^3$ cells/cm^2 cells, cultured until reaching 90% of confluency then differentiated. Three experimental conditions were established: (i) BM-MSCs maintained with complete αMEM (proliferative condition) (ii) BM-MSC cultured in complete Adipogenic Differentiation Medium (differentiated condition), (iii) BM-MSC cultured in complete Adipogenic Differentiation Medium in the presence of rhChi3L1 (100ng/ml) (differentiated Chi3L1 treated condition). For all conditions, the medium was replaced every three days, maintaining the corresponding treatment or vehicle control. At the end of differentiation period, lipid accumulation was quantified by Oil Red O staining (530 nm), and adipogenic differentiation was assessed by RT-qPCR for *PPARG2, FABP4* and *LPL*.

For osteogenic and adipogenic assays, gene expression values were normalized to proliferating BM-MSCs.

Human immunosuppression assay and FACS analysis

Fresh peripheral blood mononuclear cells (PBMC) were freshly isolated from human healthy donors and labeled with violet proliferation Dye 450 (1:1000 in PBS) for 20mins at 37°C, (BD biosciences, CA, USA), according to the manufacturer's instructions. PBMCs were then activated with phytohemagglutinin (PHA; 5µg/ml; Thermo Fisher Scientific). Activated PBMCs were cultured with or without Chi3L1-pretreated MSCs or not. Co-culture were conducted at a 1:10 MSC:PBMC ratio in mixed lymphocyte reaction medium (MLR) containing Iscove's Modified Dulbecco's Medium (IMDM) supplemented with 10% of fetal calf serum (Biosera, France), 1% of penicillin/streptomycin, 1% non-essential amino acids (Thermo Fisher Scientific), 1% glutamine (Thermo Fisher Scientific), 1% sodium pyruvate (Thermo Fisher Scientific), 2% HEPES buffer solution (Thermo Fisher Scientific), 0,1% 2-Mercaptoethanol (Gibco, Thermo Fisher Scientific). After 96 h, non-activated, activated PBMCs cultured with or without Chi3L1-vs-vehicle-pretreated MSCs were harvested and stained with the cell viability dye (FVS780, BD biosciences, CA, USA). In parallel, cells were labeled with intracellular and extracellular staining against CD4, as antibodies against CD8. Then flux cytometry was assessed to quantify total PBMCs CD4 + and CD8 + T cell and their subpopulations proliferation. To measure BM-MSC immunuspression ability, the percentage of PBMC proliferation in co-culture was compared to the proliferation of PHA-activated PBMC alone (set to 100%).

For PD-L1 and PD-L2 effect, following end of the treatment, BM-MSCs were collected and part of it were incubated with Viability marker (1:1000) at RT for 15 mins, cells were washed then incubated with 250 ng of APC-coupled anti-CD274 (PD-L1) antibody or PE-coupled-anti-CD273 (PD-L2) isotype on ice, in the dark for 30 min at 4°C. Then, cells were washed twice with PBS/1% BSA and resuspend in 500 µL of this buffer before analysis in Cytek Aurora spectral cytometry system (Cytek Biosciences) and analysis with the FlowJo software.

Murine neutralizing anti-Chi3L1 production

For in vivo studies, an anti-HEL mouse IgG2b isotype control (B478001; abinvivo) or containing the heavy and light variable domains encoding sequences of the human neutralizing Chi3L1-specific antibody (patent number: US20230406958A1) was produced in CHO cells, protein A purified with a final endotoxin level < 1EU/mg and a purity > 95% (Biointron).

Animal experiments

Animal experiments were performed in accordance with the European guidelines (directive 2010/63/EU) then were approved by the Languedoc-Roussillon Animal Research Ethics committee (CEEA-LR n°36), French Ministry for Higher Education and Research (project #32846), and French Health Authorities (Animal facility agreement C34-172-36). C57BL/6J male mice were purchased from Janvier labs, group-housed and maintained under specific pathogen-free conditions with ad libitum access to food and

water. Animals reaching predefined humane endpoints were excluded according to AVMA recommendations. Two OA preclinical model have been explored:

Collagenase-induced osteoarthritis (CiOA)

Experimental OA was induced in 10-12-week-old mice by intra-articular injection of 1 U *Clostridium histolyticum* collagenase type VII (Sigma-Aldrich) in 5 µL PBS into the left knee on days 0 and 2 under isoflurane anesthesia. The contralateral knee received 5 µL sterile 0.9% NaCl. Mice were euthanized on day 42 for histological, micro-CT, transcriptomic, and plasma analyses. For senomorphic treatment, metformin (1.33 g/L; Merck) was administered in drinking water from day 10 until euthanasia, with fresh solution replaced daily. To evaluate the functional consequences of CHI3L1 conditioning, BM-MSCs were expanded ex vivo and cultured in the presence or absence of recombinant murine CHI3L1 (100 ng/mL). On day 7 (5 days after second colVII injection), 2.5×10^5 untreated or CHI3L1-preconditioned murine BM-MSCs suspended in 7 µL 0.9% NaCl solution were injected intra-articularly into OA knees. Few hours before injection, the cells were freshly resuspended in sterile 0.9% NaCl at a density of $3.5x10^4$cell/µl. Control animals received vehicles alone.

Spontaneous age-associated osteoarthritis

Anti-Chi3L1 antibody and its matched IgG2b isotype were checked for their specifity and neutralization abilities in-vitro (Data not shown) before proceeding the *in vivo* injection. To evaluate therapeutic CHI3L1 neutralization, 70-week-old C57BL/6J mice received intraperitoneal injections of anti-Chi3L1 antibody (5 mg/kg; Biointron) or matched IgG2b isotype control every three days for a total of four injections. Between the third and fourth antibody administrations, mice received a single intra-articular injection of either BM-MSCs (2.5×10^5 cells in 7 µL sterile saline solution) or vehicle, generating four treatment groups: (i) diseased control: IgG2b isotype i.p injected vs NaCl i.a injected (ii) MSCs alone: IgG2b isotype i.p injected vs MSCs i.a injected (iii) Anti-Chi3L1 alone: anti-Chi3L1 i.p injected vs NaCl i.a injected (iiii) combination: anti-Chi3L1 i.p injected vs MSCs i.a injected. Behavioral analyses were performed before treatment initiation and before euthanasia. Mice were euthanized one month following MSC administration, plasma and knee joints were collected for histological, micro-CT, transcriptomic, and molecular analyses.

Bone parameter analysis

The tibia and femur of the hind limbs were dissected to remove overlying soft tissues.

For the CiOA (Fig. 1), CiOA; Metformine (Fig. 2), CiOA; BM-MSC; Chi3L1-pretreteated-BM-MSC (Fig. 5), tissues were scanned with a micro-computed tomography (micro-CT) scanner SkyScan 1176 (Bruker, Belgium, 0.5 mm aluminum filter, 45 kV, 500 µA, 18 µm resolution, 0.5° rotation angle) for structural analysis. Scans were reconstructed using CTAn v1.9, Nrecon v1.6 (Bruker, Belgium) and a three-dimensional (3D) model visualization software program (CTVol v2.0). Misalignment compensation, ring artifacts and beam hardening were adjusted to obtain the correct reconstruction of each paw. Bone degradation was quantified in subchondral bone and the epiphysis region of the medial and/or lateral

plateau for each tibia (CTAn software, Bruker, Belgium). Meniscal and ligament calcifications were quantified on the entire knee joint. Reconstructed 3D images of joints were obtained using the Avizo software (Avizo Lite 9.3.0, FEI, France).

For the Aged-spontaneous model (Fig. 6) tissues were scanned using NeoScan N80 micro-CT (Milexia). Scans were performed with the following parameters: 0.5 mm aluminium filter, 67 kV, 200 µA, 6 µm voxel size, and a 0.2° rotation step. Images were reconstructed using NRecon software (version 1.7.4.2, Bruker), with correction for misalignment, ring artefacts, and beam hardening to ensure accurate reconstruction of the entire knee joint. Data were then analyzed using CTAn software (version 1.23.0.2, Bruker). Reconstructed 3D images of the joints were obtained using CTVox software (Bruker)

Safranin-O/Fast Green staining for cartilage, synovial and osteophytes analysis and scoring

For cartilage analysis, mouse knees were fixed in 4% paraformaldehyde at 4°C for 48h, washed in PBS, and then processed for routine histology. Knees were decalcified in 14% EDTA/PBS for three weeks and then paraffin-embedded. Tissue sections (5 µm) were rehydrated through a gradient of ethanol and xylene. Sections were then stained with Safranin-O/Fast Green solution to evaluate cartilage degradation. Cartilage damage was analyzed using an arbitrary score from 0 to 30, based on the OARSI cartilage OA grading system and modified by van den Berg for the assessment of murine knee joints (grading scale of 0–6 for the severity of cartilage destruction and of 0–5 for the extent of damaged cartilage surface). To score synovium tissue inflammation, a semi-quantitative scoring system was employed to evaluate synovitis with scores ranging from 0 (no thickening of the lining layer and no immune cell infiltration) to 3 (maximal observed thickening of the synovial lining layer and maximal immune cell infiltration). To grade osteophyte presence a standardized quantitative scoring system was employed to assess osteophyte severity on a scale 0–3.

Behavioral test

Global spontaneous locomotion was assessed one day (D-1) before the first antibody injection and then 1 month (D + 33) after the last antibody injection using the open field test with an infrared actimeter system (Bioseb, France). Each animal was individually placed in the middle of the square arena (40 x 40 x 30 cm) and with the photocell's beam detectors that recorded continuously and automatically the movement and the behavior for 10 min. After each animal cycle, the arena was fully cleaned via ethanol to neutralize olfactory cues. Multiple parameters were evaluated: total speed, maximum speed, lower speed, distance covered, rest (immobility) time and time spent in fast and slow movements (i.e. over or below 5 cm/s). Data acquisition and analysis were executed via the actitrack software (Bioseb). All tests were conducted during the same phase of the day/night cycle at a fixed time, to limit any bias generation or circadian influence. Data were presented as post-/pre-injection ratios for each parameter per mouse.

Blood collection and serum

Blood was collected by intracardiac puncture and transferred into heparinized tubes collection tube (BD Vacutainer). Samples were centrifugated at 3000xg for 15 mins at 4°C according to the manufacturer's instruction. The resulting serum was stored at -80°C until use. Soluble CHI3L1 measurement by Elisa (R&D biotechne, Mouse Chitinase 3-like 1/YKL-40 DuoSet ELISA #DY2649). 96 wells plates were coated with the capture antibody overnight at RT under gentle shaking. Plates were washed 3 times with a wash buffer and blocked with PBS containing 1%BSA for 1h at RT under gentle shaking. After 3 washing steps, serum samples diluted 1:160 in dilution reagent were added and incubated for 2h at RT in the dark. Wells were then washed 3 times, and streptavidine HRP was added at a dilution of 1:50. Plates were incubated for 20 mins at RT protected from light. Plates were washed and substrate solution was added, then kept in the dark for 20 min at RT under shaking condition. The enzymatic reaction has been stopped by adding a stop solution. The optical density of each well was determined using the microplate reader set to 450 and 540 nm for values correction. The values were exported to spreadsheet excel, and concentrations were calculated by applying the appropriate dilution factor.

Gene expression analysis by real-time quantitative PCR

For qPCR experiments, total RNA was extracted from cells using the RNeasy® Mini kit (Qiagen; 74106) according to the manufacturer's instructions. RNA quality was checked by spectral analysis (A260/280 nm), and then samples were stored at − 80°C. Reverse transcription was performed using the M-MLV reverse transcriptase (Invitrogen; 28025013; 5U/µL final concentration), 500ng total RNA, a random hexamer primer (Thermo Scientific, GER; S0142; 10ng/µL final concentration), and DNTPs (Roche, CH; 1 277 049; 5mM final concentration) in M-MLV reverse transcriptase buffer (Invitrogen; 18057-018), for a total volume of 20µL. SYBR Green-based quantitative PCR was performed using the LightCycle® 480 SYBR Green I master reaction mix (Roche, 04707516001), 10 ng of cDNA, and the LightCycler 480 real-time PCR system (Roche) (40 cycles of amplification). Raw data (Ct values) were analyzed using the comparative Ct method. Gene expression data were calculated as relative to the expression of housekeeping genes. The comparative threshold cycle method (ΔΔCT) was used to quantify relative gene expression, and the obtained quantification was transformed to exponential 2 − ΔΔCT values. A p-value below 0.05 (Student's t-test or one-way ANOVA) was considered as statistically significant. Primers sequences used for RT-qPCR are listed in Supplementary Table 1.

Protein isolation and Western blotting

For all BM-MSCs samples, proteins were extracted using the appropriate volume of Lysis buffer 17 (R&D systems; 895943), supplemented with protease inhibitors (Roche; 11 873 580 001), according to the manufacturer's instructions. Protein concentration was determined by BCA Protein assay (Fisher Scientific #10678484), proteins were denatured in Laemmli blue with beta-mercaptoethanol (at 95°C, for 10min). An equal amount of 33 µg of total protein was subsequently resolved with Mini-PROTEAN® TGX™ 4 to 15% gradient gels (Bio-Rad #456–1084) in Tris-glycine running buffer. Gels were transferred onto polyvinylidene fluoride membranes (Bio-Rad Transblot® Turbo™ #170–4157) previously activated in methanol using Transblot® Turbo™ transfer system. PVDF membranes were blocked for 1h at RT with

5% milk solution (TBS with 5% skimmed milk and 0.1% Tween-20, boiled and filtered), followed by a 4°C overnight incubation with primary antibodies with gentle agitation. The following primary antibodies used: IgG anti-human p16 (1:750 in 5% Skimmed milk-TBST, Proteintech; 10883-1-AP), and IgG anti-HSP90 (1:3000 in 3% BSA-TBST, Cell signaling: #4877), serving as loading control. Membranes were washed 3 × 15 min with TBST then incubated for 1h at RT with HRP-conjugated secondary antibodies with gentle agitation. The secondary antibody used: goat anti-rabbit IgG (1:2000 in 5% BSA-TBST; Cell Signaling #7074) or goat anti-mouse IgG (1:2000 in 5% BSA-TBST, Cell Signaling #7076). Then, membranes were washed three times with TBST for 5 mins each before soaked in Pierce™ ECL Western Blotting Substrate (Thermoscientific #32106). Chemiluminescent signals were detected by Bio-Rad ChemiDoc™ MP XRS+ Imaging System (Bio-Rad). Bands intensities were quantified by Image lab software (Bio-Rad).

Incucyte® Chemotaxis Cell Migration Assay

After treatment, BM-MSCs were collected, counted and 2.5k cells were placed into Incucyte® Clearview Reservoir Plate (Sartorius # 4600) in a Incucyte® Clearview 96-Well plate (Sartorius, #4582). Wells were filled with DMEM supplemented with L-glu and penicylin streptomycine without FBS in presence or absence of the chemoattractant CXCL11 (SDF1alpha used at 120ng/ml). 4 experimental conditions were tested: (i) untreated BM-MSCs without chemoattractant supplementation, (ii) Chi3L1 pretreated BM-MSCs with chemoattractant supplementation (iii) untreated BM-MSCs with chemoattractant supplementation (iiii) Chi3L1 pretreated BM-MSC with chemoattractant supplementation. The plate was incubated in the Incucyte® Live-Cell Analysis System at 37°C for 24hours, images of wells were acquired each 2 hours. Cell migration and dynamics were quantified via Incucyte® Chemotaxis Analysis Software Module (Sartorius # 9600-0015)

Supernatant soluble cytokine quantification

For BM-MSCs untreated vs treated with rhChi3L1, conditioned media were collected 48 h upon the end of treatment. Cytokine concentrations were carried on by the bead-based multiplex assay, LEGENDplex Human Essential Immune Response Panel kit (13-plex: IL-1β, IL-2, IL-4, IFN-γ, TNF-α, MCP-1 (CCL2), CXCL10, IL-6, IL-8 (CXCL8), IL-10, IL-12p70, IL-17A and Free Active TGF-β1) (Bio-Legend, #740930) according to the manufacturer's instructions. Samples were diluted 1:1 in an assay buffer prior to analysis and acquired on a Acea NovoCyte® Flow Cytometer (Agilent Technologies). Data were analyzed and cytokine concentrations were calculated using LEGENDplex (BioLegend) v.8 software.

Metabolomics analysis:

An equal count ($1x10^6$ cell) of Chi3L1 pretreated/untreated BM-MSCs derived from 3 different biological donors were harvested and prepared for metabolomic profiling by MAMMA platform (IRCM-Montpellier-France). Briefly, cells were lyzed and subjected to metabolite precipitation, centrifugation and concentration. Metabolites were isolated by chromatography and analysed by mass spectrometry. Metabolites levels were determined using corrected data values. Internal standards were used for quality control and correction of the measured metabolite signals. Metabolite abundances were determined

from the corrected data values ($p < 0.05$). Given the inter-individual quantitative variability, only metabolites showing a same consistent behavior following Chi3L1 treatment across the three biological MSC replicates were considered.

NULISA immunoassay

NULISA experiments were performed with Mouse Panel (800153, Alamar Biosciences) according to manufacturer's instructions. Briefly, sample were centrifuged to remove residuals 10 min, 10 000 g and 25µL were transferred on assay plate. Reagent plates were homogenized with 15 upside-down rotations, and then centrifuged with sample and library 20 sec, 352 g before loading onto the ARGO HT System. After run, prepared sequencing library tube was stored until sequencing at -20°C. Finally, 3µL of NULISA sequencing library was used to determine DNA concentration using Qubit™ dsDNA HS Assay kit (Invitrogen by Thermo Fisher Scientific,USA) with QFX spectrofluorometer (DeNovix Inc.™, USA). Library was then sequenced using NextSeq 500/550 High Output Kit v2.5 (20024906, Illumina) onto Illumina NextSeq 550 System. The output file was then processed by Alamar cloud system to generate NPQ brut data.

Data collection and bioinformatics

For synovial single-cell RNA-seq data, public RNA-seq data were recovered from the original study[127]. Fastq files were downloaded from NCBI GEO, accession GSE152805. In total, 10,640 synovial tissue cells were analyzed. After quality control and normalization, dimensionality reduction was conducted using principal component analysis (PCA) followed by Uniform Manifold Approximation and Projection (UMAP) to illustrate the transcriptional landscape of synovial cells. Cells were grouped into an optimal number of clusters using Seurat package and cluster annotation was performed using the celldex R package was used. The top upregulated genes for cell sub-clusters were clusters were identified based on markers reported in the original study, allowing the synovial cell populations. To evaluate the spatial distribution of *CHI3L1, i*ts expression was mapped onto the UMAP projection to visualize its localization across synovial tissue cells. Moreover, *CHI3L1* levels were quantified across annotated cell populations to assess differences in expression among cell subpopulations. For differential transcriptomic gene expression analysis of chronological and replicative MSC ageing, publicly available Affymetrix data were downloaded and Illumina pipeline were applied on raw data to obtain significant signals for each probe set ($p < 0.05$). A common gene set signature between aged and senescent MSCs was obtained after normalization and differential expression using matched-pair analysis as previously described[128]. Fastq files were downloaded from NCBI GEO, accession GSE12274 for MSCs donor age and GSE9593 for MSCs replicative senescence MSC.

Statistical analysis

All data are presented mean ± SEM. Unpaired or paired conditions were properly applied. Normality and lognormality tests were assessed to identify parametric and non-parametric settings according to the

experimental conditions. Tests were used The Student's *t*-test was used for comparisons between experimental groups, and multiple t-tests or ANOVA were conducted for multiple comparisons. All heatmaps were generated in R (RStudio.app 2026), raw values were converted into log2 then Z score. Prior to visualization data were standardized using z-score transformation. n referred distinct independent biological replicates. For mathematical correlations and linear regressions, data obtained from samples were blasted and Pearson r coefficient was calculated for appropriate parameters. Data were analyzed using the Prism software v11 (GraphPad Software Inc.); p-values < 0.05 were considered significant (*p < 0.05; **p < 0.01; ***p < 0.001; ****p < 0.0001).

Declarations

Ethical approval and consent to participate

Informed consent was obtained from all subjects involved in the study. The study was conducted in accordance with the Declaration of Helsinki and approved by (1) the Regional Investigational Review Board "Comité de Protection des Personnes SUDEST II, Lyon, France" (Protocol 2019-A01067-50 approved on September 11th, 2019) and (2) Regional Investigation Review board Montpellier (number approval IRB-MTP_2022_11_202201238). IRB Accreditation number: 198711 under the title: Consolidation of biological collections with a view to a harmonized approach to research into rheumatological diseases and approved on November 28th, 2022.

CONSENT FOR PUBLICATION

All authors agree to publish this version of the article

COMPETING INTERESTS

All other authors declare that they have no competing or a conflict of interests.

ARTIFICIAL INTELLIGENCE

The authors declare that Artificial Intelligence was used for English grammatical and sentence correction

CONTRIBUTION

Conceptualization: G.M., YM.P., J.M.B.

Formal analysis: G.M., A.L.B, R.S., C.T., C.P., C.A., C.C.

Investigation: G.M., A.L.B., R.S., C.T., C.P., C.A., B.R., C.J., F.D., Y.M.P., J.M.B.

Methodology: G.M., Y.M.P., J.M.B.

Project administration: G.M., Y.M.P., J.M.B.

Supervision: Y.M.P., J.M.B.

Visualization: G.M., Y.M.P, J.M.B.

Writing-original draft: G.M.

Reviewing, correcting and editing: G.M., A.L.B., R.S., C.T., C.P., C.A., B.R., D.D.S., F.D.C., P.P., C.J., F.D., Y.M.P., J.M.B.

ACKNOWLEDGEMENT

We thank Yassin Tachikart, Audrey Sansolini, Margot Milano, Olivier Malaise, Marion Loivet & Clara Taffoni for their technical supports in this study. We acknowledge the professional help of animal facilities RAM platform (Denis Greuet, Antoine Picot), the Histology facility RHEM (Nelly Pirot), ECELLFRANCE non-clinical platform (a national infrastructure supported by the PLF172 - Alexia Gilles, Claire Abeza), the PPC platform (Christophe Hirtz, Nicolas Pradeilles), the CHU transcriptomic platform (Said Assou, Brice Dupuy) the MAMMA platform, the BGI and the BioIntron company,

Special thanks to (1) the Orthopedic department directed by Pr Louis Dagneaux. (2) Sophie Grasset from the Rheumatology department located at CHU Lapeyronie, Montpellier, France to provide clinical data and patient signed consents. (3) all the IRMB-personal and teams for their fruitful discussion and critical comments (Martine Daujat, Sabine Gerbal, Maria del Mar Naranjo Gomez, Gabriel Courties, Maroun Khoury, Salwa Sebti, Mehdi Benamar) (4) Dr. Daujat and Dr. Gerbal for providing the MEF cells and (5) for all the ISRID team.

FUNDING

This work was supported by a research grant from French society of rheumatology (SFR), Avenir foundation, Défi clef, CHU Montpellier-Tremplin and the support of Immun4Cure University Hospital Institute "Institute for innovative immunotherapies in autoimmune diseases" (France 2030 /ANR-23-IAHU-009) and AVIESAN-Servier. J.M.B. and Y.M.P. works were supported by Défi Clé “Biothérapies” INSERM/Région Occitanie, CHU Montpellier-Tremplin, Montpellier University, INSERM AGEMED Program, Oscar Grant, Avenir foundation and SFR emergence program 2023. G.M is a recipient of the Ph.D program from Montpellier University. G.M. received the Ph.D 4th year personal fellowship from SFR-2025-2026 grant program.

FIGURE ARTWORK

Figure artwork was created with BioRender licence to INSERM-U1183 IRMB

DATA AND MATERIALS AVAILABILITY

The raw data of synovial are available online: ArrayExpress accession: E-MTAB-17452

References

1. Steinmetz, J. D. *et al.* Global, regional, and national burden of osteoarthritis, 1990–2020 and projections to 2050: a systematic analysis for the Global Burden of Disease Study 2021. *The Lancet Rheumatology* 5, e508–e522 (2023).
2. Maroun, G., Fissoun, C., Villaverde, M., Brondello, J.-M. & Pers, Y.-M. Senescence-regulatory factors as novel circulating biomarkers and therapeutic targets in regenerative medicine for osteoarthritis. *Joint Bone Spine* 91, 105640 (2024).
3. Huang, Y.-Z. *et al.* Mesenchymal Stem/Progenitor Cells Derived from Articular Cartilage, Synovial Membrane and Synovial Fluid for Cartilage Regeneration: Current Status and Future Perspectives. *Stem Cell Rev Rep* 13, 575–586 (2017).
4. Bernardo, M. E. & Fibbe, W. E. Mesenchymal stromal cells: sensors and switchers of inflammation. *Cell Stem Cell* 13, 392–402 (2013).
5. Sagaradze, G. D., Basalova, N. A., Efimenko, A. Y. & Tkachuk, V. A. Mesenchymal Stromal Cells as Critical Contributors to Tissue Regeneration. *Front Cell Dev Biol* 8, 576176 (2020).
6. Ayala-Cuellar, A. P., Kang, J.-H., Jeung, E.-B. & Choi, K.-C. Roles of Mesenchymal Stem Cells in Tissue Regeneration and Immunomodulation. *Biomol Ther (Seoul)* 27, 25–33 (2019).
7. Maxson, S., Lopez, E. A., Yoo, D., Danilkovitch-Miagkova, A. & Leroux, M. A. Concise review: role of mesenchymal stem cells in wound repair. *Stem Cells Transl Med* 1, 142–149 (2012).
8. Li, Y. *et al.* SOD2 promotes the immunosuppressive function of mesenchymal stem cells at the expense of adipocyte differentiation. *Mol Ther* 32, 1144–1157 (2024).
9. Tabet, C. G. *et al.* Advanced therapy with mesenchymal stromal cells for knee osteoarthritis: Systematic review and meta-analysis of randomized controlled trials. *J Orthop Translat* 48, 176–189 (2024).
10. Chu, H. *et al.* Comparison studies identify mesenchymal stromal cells with potent regenerative activity in osteoarthritis treatment. *NPJ Regen Med* 9, 14 (2024).
11. Pers, Y.-M. *et al.* Effect of intra-articular adipose-derived mesenchymal stromal cell versus placebo injection on pain and function in patients with knee osteoarthritis: the ADIPOA2 phase 2b randomised clinical trial. *Ann Rheum Dis* 84, 2103–2114 (2025).
12. Cao, M. *et al.* Efficacy and safety of mesenchymal stem cells in knee osteoarthritis: a systematic review and meta-analysis of randomized controlled trials. *Stem Cell Res Ther* 16, 122 (2025).
13. Dai, W. *et al.* Intra-Articular Mesenchymal Stromal Cell Injections Are No Different From Placebo in the Treatment of Knee Osteoarthritis: A Systematic Review and Meta-analysis of Randomized Controlled Trials. *Arthroscopy* 37, 340–358 (2021).
14. Maroun, G., Brondello, J.-M. & Pers, Y.-M. Strategies to overcome the full potential of mesenchymal stromal cells (MSCs) for the treatment of osteoarthritis and cartilage regeneration. *Joint Bone Spine* 93, 106074 (2026).

15. Brunet, A., Goodell, M. A. & Rando, T. A. Ageing and rejuvenation of tissue stem cells and their niches. *Nat Rev Mol Cell Biol* 24, 45–62 (2023).
16. Kennedy, B. K. *et al.* Geroscience: linking aging to chronic disease. *Cell* 159, 709–713 (2014).
17. Brunauer, R., Alavez, S. & Kennedy, B. K. Stem Cell Models: A Guide to Understand and Mitigate Aging? *Gerontology* 63, 84–90 (2017).
18. Oh, J., Lee, Y. D. & Wagers, A. J. Stem cell aging: mechanisms, regulators and therapeutic opportunities. *Nat Med* 20, 870–880 (2014).
19. van Deursen, J. M. The role of senescent cells in ageing. *Nature* 509, 439–446 (2014).
20. López-Otín, C., Blasco, M. A., Partridge, L., Serrano, M. & Kroemer, G. Hallmarks of aging: An expanding universe. *Cell* 186, 243–278 (2023).
21. González-Gualda, E., Baker, A. G., Fruk, L. & Muñoz-Espín, D. A guide to assessing cellular senescence *in vitro* and *in vivo*. *The FEBS Journal* 288, 56–80 (2021).
22. McHugh, D. & Gil, J. Senescence and aging: Causes, consequences, and therapeutic avenues. *J Cell Biol* 217, 65–77 (2018).
23. Kuilman, T. & Peeper, D. S. Senescence-messaging secretome: SMS-ing cellular stress. *Nat Rev Cancer* 9, 81–94 (2009).
24. Wang, B., Han, J., Elisseeff, J. H. & Demaria, M. The senescence-associated secretory phenotype and its physiological and pathological implications. *Nat Rev Mol Cell Biol* 25, 958–978 (2024).
25. De Magalhães, J. P. Cellular senescence in normal physiology. *Science* 384, 1300–1301 (2024).
26. Valdivieso, K. *et al.* Transcription-independent induction of rapid-onset senescence is integral to healing. *Nat Cell Biol* 28, 1281–1299 (2026).
27. Ritschka, B. *et al.* The senescence-associated secretory phenotype induces cellular plasticity and tissue regeneration. *Genes Dev* 31, 172–183 (2017).
28. Ajoolabady, A. *et al.* Hallmarks and mechanisms of cellular senescence in aging and disease. *Cell Death Discov.* 11, 364 (2025).
29. Childs, B. G., Durik, M., Baker, D. J. & van Deursen, J. M. Cellular senescence in aging and age-related disease: from mechanisms to therapy. *Nat Med* 21, 1424–1435 (2015).
30. Huang, W., Hickson, L. J., Eirin, A., Kirkland, J. L. & Lerman, L. O. Cellular senescence: the good, the bad and the unknown. *Nat Rev Nephrol* 18, 611–627 (2022).
31. Jeon, O. H. *et al.* Local clearance of senescent cells attenuates the development of post-traumatic osteoarthritis and creates a pro-regenerative environment. *Nat Med* 23, 775–781 (2017).
32. Gil, T.-H. *et al.* Senolytic drugs relieve pain by reducing peripheral nociceptive signaling without modifying joint tissue damage in spontaneous osteoarthritis. *Aging (Albany NY)* 14, 6006–6027 (2022).
33. Endo, K., Ozeki, N., Koga, H. & Sekiya, I. Piperlongumine attenuates knee osteoarthritis progression by eliminating senescent meniscus cells and chondrocytes. *Biochem Biophys Res Commun* 829, 154179 (2026).

34. Chen, L. *et al.* Daucosterol alleviates osteoarthritis by targeting chondrocyte senescence via inhibiting of the JNK pathway. *International Immunopharmacology* 175, 116450 (2026).
35. Peng, W. *et al.* Synergistic targeting of senolytic and senomorphic action with dual-engineered biomimetic macrophage nanovesicles for mitigating osteoarthritis. *Bioact Mater* 60, 20–39 (2026).
36. Peilin, W. *et al.* Directed elimination of senescent cells attenuates development of osteoarthritis by inhibition of c-IAP and XIAP. *Biochim Biophys Acta Mol Basis Dis* 1865, 2618–2632 (2019).
37. Zhao, X. *et al.* Targeting p21-Positive Senescent Chondrocytes via IL-6R/JAK2 Inhibition to Alleviate Osteoarthritis. *Adv Sci (Weinh)* 12, e2410795 (2025).
38. Chen, X. *et al.* Specific Clearance of Senescent Synoviocytes Suppresses the Development of Osteoarthritis based on Aptamer-Functionalized Targeted Drug Delivery System. *Adv Funct Materials* 32, 2109460 (2022).
39. Feng, X. *et al.* Metformin attenuates cartilage degeneration in an experimental osteoarthritis model by regulating AMPK/mTOR. *Aging (Albany NY)* 12, 1087–1103 (2020).
40. Li, P. L. *et al.* Multiomic identification of senescent stem cell populations critical for osteoarthritis progression and therapy in subchondral bones. *Sci Adv* 11, eadu2294 (2025).
41. Jayasuriya, C. T. *et al.* Molecular characterization of mesenchymal stem cells in human osteoarthritis cartilage reveals contribution to the OA phenotype. *Sci Rep* 8, 7044 (2018).
42. Raut, R. *et al.* Constructing a cross-tissue human knee single-cell atlas identified osteoarthritis reduces regenerative tissue stem cells while increasing inflammatory pain macrophages. Preprint at https://doi.org/10.21203/rs.3.rs-6247502/v1 (2025).
43. Fan, M. *et al.* Detrimental alteration of mesenchymal stem cells by an articular inflammatory microenvironment results in deterioration of osteoarthritis. *BMC Med* 21, 215 (2023).
44. Malaise, O. *et al.* Mesenchymal stem cell senescence alleviates their intrinsic and seno-suppressive paracrine properties contributing to osteoarthritis development. *Aging* 11, 9128–9146 (2019).
45. Yang, D. *et al.* Senescent bone marrow mesenchymal stem cells exacerbate subchondral bone sclerosis and osteoarthritis via the senescence-associated secretory phenotype. *Stem Cell Res Ther* 16, 699 (2025).
46. Bojesen, S. E., Johansen, J. S. & Nordestgaard, B. G. Plasma YKL-40 levels in healthy subjects from the general population. *Clinica Chimica Acta* 412, 709–712 (2011).
47. Lehallier, B. *et al.* Undulating changes in human plasma proteome profiles across the lifespan. *Nat Med* 25, 1843–1850 (2019).
48. Nishimura, N. *et al.* Chitinase 3-like 1 is a profibrogenic factor overexpressed in the aging liver and in patients with liver cirrhosis. *Proc. Natl. Acad. Sci. U.S.A.* 118, e2019633118 (2021).
49. Taifour, T. *et al.* The CHI3L1-neutrophil axis drives immune suppression and breast cancer metastatic dissemination. *JCI Insight* 11, e199307 (2026).
50. Sanfilippo, C. *et al.* Sex difference in CHI3L1 expression levels in human brain aging and in Alzheimer's disease. *Brain Res* 1720, 146305 (2019).

51. Kato, S. *et al.* Role of Chitinase 3-like-1 in Myelofibrosis via Fibroblast-Produced Extracellular Matrix Enhancement. *J Cell Physiol* 241, e70166 (2026).
52. Cai, Q. *et al.* Explainable machine learning incorporating CHI3L1 enhances liver fibrosis staging in chronic hepatitis B: The CHILI multicenter study. *Dig Liver Dis* 58, 925–934 (2026).
53. Guan, J. *et al.* Increased Synovial Fluid YKL-40 Levels are Linked with Symptomatic Severity in Knee Osteoarthritis Patients. *Clin Lab* 61, 991–997 (2015).
54. Väänänen, T. *et al.* YKL-40 as a novel factor associated with inflammation and catabolic mechanisms in osteoarthritic joints. *Mediators Inflamm* 2014, 215140 (2014).
55. Conrozier, T. Serum levels of YKL-40 and C reactive protein in patients with hip osteoarthritis and healthy subjects: a cross sectional study. *Annals of the Rheumatic Diseases* 59, 828–831 (2000).
56. He, C. H. *et al.* Chitinase 3-like 1 regulates cellular and tissue responses via IL-13 receptor α2. *Cell Rep* 4, 830–841 (2013).
57. Yang, X. *et al.* CHI3L1/YKL-40 signaling inhibits neurogenesis in models of Alzheimer's disease. *Sci. Adv.* 11, eadv1492 (2025).
58. Zheng, Q. *et al.* Decoding the CHI3L1/IL-13Rα2 signaling nexus in MASH-fibrosis pathogenesis. *Sci Adv* 11, eadz3223 (2025).
59. Fissoun, C. *et al.* The ganglioside GD3 and its synthase (ST8SIA1) as novel senescence markers associated with osteoarthritis. *Geroscience* 48, 2013–2027 (2026).
60. Aref-Eshghi, E. *et al.* Overexpression of MMP13 in human osteoarthritic cartilage is associated with the SMAD-independent TGF-β signalling pathway. *Arthritis Res Ther* 17, 264 (2015).
61. Swahn, H. *et al.* Senescent cell population with ZEB1 transcription factor as its main regulator promotes osteoarthritis in cartilage and meniscus. *Ann Rheum Dis* 82, 403–415 (2023).
62. Yan, J., Feng, G., Ma, L., Chen, Z. & Jin, Q. Metformin alleviates osteoarthritis in mice by inhibiting chondrocyte ferroptosis and improving subchondral osteosclerosis and angiogenesis. *J Orthop Surg Res* 17, 333 (2022).
63. Kang, Y. *et al.* Association of metformin with osteoarthritis progression and total joint arthroplasty: evidence from the UK Biobank, a large population-based cohort study. *Clin Rheumatol* 45, 5063–5073 (2026).
64. Pan, F. *et al.* Metformin for Knee Osteoarthritis in Patients With Overweight or Obesity: A Randomized Clinical Trial. *JAMA* 333, 1804 (2025).
65. Li, H. *et al.* Exploration of metformin as novel therapy for osteoarthritis: preventing cartilage degeneration and reducing pain behavior. *Arthritis Res Ther* 22, 34 (2020).
66. Wagner, W. *et al.* Aging and replicative senescence have related effects on human stem and progenitor cells. *PLoS One* 4, e5846 (2009).
67. Lai, Y. *et al.* Kindlin-2 loss in condylar chondrocytes causes spontaneous osteoarthritic lesions in the temporomandibular joint in mice. *Int J Oral Sci* 14, 33 (2022).

68. Wu, X. *et al.* Kindlin-2 preserves integrity of the articular cartilage to protect against osteoarthritis. *Nat Aging* 2, 332–347 (2022).
69. Ren, X. *et al.* Maintenance of Nucleolar Homeostasis by CBX4 Alleviates Senescence and Osteoarthritis. *Cell Rep* 26, 3643–3656.e7 (2019).
70. Karalilova, R., Kazakova, M., Batalov, A. & Sarafian, V. Correlation between protein YKL-40 and ultrasonographic findings in active knee osteoarthritis. *Med Ultrason* 1, 57–63 (2018).
71. Ambrosi, T. H. *et al.* Aged skeletal stem cells generate an inflammatory degenerative niche. *Nature* 597, 256–262 (2021).
72. Ryan, P. C. *et al.* Acute and chronic bioeffects of single and multiple doses of piezoelectric shockwaves (EDAP LT.01). *J Urol* 145, 399–404 (1991).
73. Moerman, E. J., Teng, K., Lipschitz, D. A. & Lecka-Czernik, B. Aging activates adipogenic and suppresses osteogenic programs in mesenchymal marrow stroma/stem cells: the role of PPAR-gamma2 transcription factor and TGF-beta/BMP signaling pathways. *Aging Cell* 3, 379–389 (2004).
74. Stolzing, A., Jones, E., McGonagle, D. & Scutt, A. Age-related changes in human bone marrow-derived mesenchymal stem cells: consequences for cell therapies. *Mech Ageing Dev* 129, 163–173 (2008).
75. Bustos, M. L. *et al.* Aging mesenchymal stem cells fail to protect because of impaired migration and antiinflammatory response. *Am J Respir Crit Care Med* 189, 787–798 (2014).
76. Contreras-Lopez, R. *et al.* The ATP synthase inhibition induces an AMPK-dependent glycolytic switch of mesenchymal stem cells that enhances their immunotherapeutic potential. *Theranostics* 11, 445–460 (2021).
77. Li, H., Dai, H. & Li, J. Immunomodulatory properties of mesenchymal stromal/stem cells: The link with metabolism. *J Adv Res* 45, 15–29 (2023).
78. Fang, J. *et al.* NAD+ salvage governs the immunosuppressive capacity of mesenchymal stem cells. *Cell Mol Immunol* 20, 1171–1185 (2023).
79. Gnani, D. *et al.* An early-senescence state in aged mesenchymal stromal cells contributes to hematopoietic stem and progenitor cell clonogenic impairment through the activation of a pro-inflammatory program. *Aging Cell* 18, e12933 (2019).
80. Chen, D. *et al.* Bone marrow-derived mesenchymal stem cells promote cell proliferation of multiple myeloma through inhibiting T cell immune responses via PD-1/PD-L1 pathway. *Cell Cycle* 17, 858–867 (2018).
81. Gao, Y. *et al.* Multi-omics analysis of human mesenchymal stem cells shows cell aging that alters immunomodulatory activity through the downregulation of PD-L1. *Nat Commun* 14, 4373 (2023).
82. Davies, L. C., Heldring, N., Kadri, N. & Le Blanc, K. Mesenchymal Stromal Cell Secretion of Programmed Death-1 Ligands Regulates T Cell Mediated Immunosuppression. *Stem Cells* 35, 766–776 (2017).

83. Niu, J., Yue, W., Le-Le, Z., Bin, L. & Hu, X. Mesenchymal stem cells inhibit T cell activation by releasing TGF-β1 from TGF-β1/GARP complex. *Oncotarget* 8, 99784–99800 (2017).
84. Di Nicola, M. *et al.* Human bone marrow stromal cells suppress T-lymphocyte proliferation induced by cellular or nonspecific mitogenic stimuli. *Blood* 99, 3838–3843 (2002).
85. Terraza-Aguirre, C. *et al.* PPARβ/δ priming enhances mesenchymal stromal cell anti-apoptotic properties on chondrocytes via ANGPTL4 and improves their therapeutic effects in osteoarthritis. *Stem Cells Transl Med* 15, szag053 (2026).
86. ter Huurne, M. *et al.* Antiinflammatory and chondroprotective effects of intraarticular injection of adipose-derived stem cells in experimental osteoarthritis. *Arthritis Rheum* 64, 3604–3613 (2012).
87. Schelbergen, R. F. *et al.* Treatment efficacy of adipose-derived stem cells in experimental osteoarthritis is driven by high synovial activation and reflected by S100A8/A9 serum levels. *Osteoarthritis Cartilage* 22, 1158–1166 (2014).
88. Tejedor, G. *et al.* MANF Produced by MRL Mouse-Derived Mesenchymal Stem Cells Is Pro-regenerative and Protects From Osteoarthritis. *Front Cell Dev Biol* 9, 579951 (2021).
89. Maumus, M. *et al.* Utility of a Mouse Model of Osteoarthritis to Demonstrate Cartilage Protection by IFNγ-Primed Equine Mesenchymal Stem Cells. *Front Immunol* 7, 392 (2016).
90. Ivanovska, A. *et al.* Identification of disease-stage therapeutic responses of mesenchymal stromal cells retrieved from murine osteoarthritic joints. *Front Cell Dev Biol* 13, 1521437 (2025).
91. Zhang, S. *et al.* Role of Chitinase 3-Like 1 Protein in the Pathogenesis of Hepatic Insulin Resistance in Nonalcoholic Fatty Liver Disease. *Cells* 10, 201 (2021).
92. Lukjanenko, L. *et al.* Aging Disrupts Muscle Stem Cell Function by Impairing Matricellular WISP1 Secretion from Fibro-Adipogenic Progenitors. *Cell Stem Cell* 24, 433–446.e7 (2019).
93. Todd, H. *et al.* Wnt16 Is Associated with Age-Related Bone Loss and Estrogen Withdrawal in Murine Bone. *PLoS One* 10, e0140260 (2015).
94. Movérare-Skrtic, S. *et al.* Osteoblast-derived WNT16 represses osteoclastogenesis and prevents cortical bone fragility fractures. *Nat Med* 20, 1279–1288 (2014).
95. Jin, Y., Sun, X., Pei, F., Zhao, Z. & Mao, J. Wnt16 signaling promotes osteoblast differentiation of periosteal derived cells in vitro and in vivo. *PeerJ* 8, e10374 (2020).
96. Yu, B., Sondag, G. R., Malcuit, C., Kim, M.-H. & Safadi, F. F. Macrophage-Associated Osteoactivin/GPNMB Mediates Mesenchymal Stem Cell Survival, Proliferation, and Migration Via a CD44-Dependent Mechanism. *J Cell Biochem* 117, 1511–1521 (2016).
97. Hu, X., Zhang, P., Xu, Z., Chen, H. & Xie, X. GPNMB enhances bone regeneration by promoting angiogenesis and osteogenesis: Potential role for tissue engineering bone. *J of Cellular Biochemistry* 114, 2729–2737 (2013).
98. Sondag, G. R. *et al.* Osteoactivin inhibition of osteoclastogenesis is mediated through CD44-ERK signaling. *Exp Mol Med* 48, e257–e257 (2016).

99. McKenna, H. J. *et al.* Mice lacking flt3 ligand have deficient hematopoiesis affecting hematopoietic progenitor cells, dendritic cells, and natural killer cells. *Blood* 95, 3489–3497 (2000).
100. Momenilandi, M. *et al.* FLT3L governs the development of partially overlapping hematopoietic lineages in humans and mice. *Cell* 187, 2817–2837.e31 (2024).
101. Tsapogas, P. *et al.* In vivo evidence for an instructive role of fms-like tyrosine kinase-3 (FLT3) ligand in hematopoietic development. *Haematologica* 99, 638–646 (2014).
102. Ding, L., Saunders, T. L., Enikolopov, G. & Morrison, S. J. Endothelial and perivascular cells maintain haematopoietic stem cells. *Nature* 481, 457–462 (2012).
103. Heissig, B. *et al.* Recruitment of Stem and Progenitor Cells from the Bone Marrow Niche Requires MMP-9 Mediated Release of Kit-Ligand. *Cell* 109, 625–637 (2002).
104. Fröbel, J. *et al.* The Hematopoietic Bone Marrow Niche Ecosystem. *Front. Cell Dev. Biol.* 9, 705410 (2021).
105. Voog, J. & Jones, D. L. Stem cells and the niche: a dynamic duo. *Cell Stem Cell* 6, 103–115 (2010).
106. Fan, Y. *et al.* Unveiling inflammatory and prehypertrophic cell populations as key contributors to knee cartilage degeneration in osteoarthritis using multi-omics data integration. *Ann Rheum Dis* 83, 926–944 (2024).
107. Park, K.-R. *et al.* Chi3L1 is a therapeutic target in bone metabolism and a potential clinical marker in patients with osteoporosis. *Pharmacol Res* 184, 106423 (2022).
108. Sakata, M. *et al.* YKL-39, a human cartilage-related protein, induces arthritis in mice. *Clin Exp Rheumatol* 20, 343–350 (2002).
109. Vos, K. *et al.* Raised human cartilage glycoprotein-39 plasma levels in patients with rheumatoid arthritis and other inflammatory conditions. *Ann Rheum Dis* 59, 544–548 (2000).
110. Johansen, J. S., Kirwan, J. R., Price, P. A. & Sharif, M. Serum YKL-40 concentrations in patients with early rheumatoid arthritis: relation to joint destruction. *Scand J Rheumatol* 30, 297–304 (2001).
111. Dela Cruz, C. S. *et al.* Chitinase 3-like-1 Promotes Streptococcus pneumoniae Killing and Augments Host Tolerance to Lung Antibacterial Responses. *Cell Host & Microbe* 12, 34–46 (2012).
112. Marion, C. R. *et al.* Chitinase 3-Like 1 (Chil1) Regulates Survival and Macrophage-Mediated Interleukin-1β and Tumor Necrosis Factor Alpha during Pseudomonas aeruginosa Pneumonia. *Infect Immun* 84, 2094–2104 (2016).
113. Meng, C. *et al.* Therapeutic potential of CHI3L1 in osteoarthritis: Inhibition of cartilage matrix degradation and inflammation through TLR4-MAPK-STAT1 pathway. *Int Immunopharmacol* 156, 114684 (2025).
114. Muñoz-Espín, D. & Serrano, M. Cellular senescence: from physiology to pathology. *Nat Rev Mol Cell Biol* 15, 482–496 (2014).
115. Zhao, T., Su, Z., Li, Y., Zhang, X. & You, Q. Chitinase-3 like-protein-1 function and its role in diseases. *Sig Transduct Target Ther* 5, 201 (2020).

116. Taifour, T. *et al.* The tumor-derived cytokine Chi3l1 induces neutrophil extracellular traps that promote T cell exclusion in triple-negative breast cancer. *Immunity* 56, 2755–2772.e8 (2023).
117. Xu, W. *et al.* IL13Rα2 as a crucial receptor for Chi3l1 in osteoclast differentiation and bone resorption through the MAPK/AKT pathway. *Cell Commun Signal* 22, 81 (2024).
118. Di Rosa, M. *et al.* Determination of chitinases family during osteoclastogenesis. *Bone* 61, 55–63 (2014).
119. Gao, L., Lee, H., Goodman, J. H. & Ding, L. Hematopoietic stem cell niche generation and maintenance are distinguishable by an epitranscriptomic program. *Cell* 187, 2801–2816.e17 (2024).
120. Schlegelmilch, K. *et al.* WISP 1 is an important survival factor in human mesenchymal stromal cells. *Gene* 551, 243–254 (2014).
121. Li, B. *et al.* The melanoma-associated transmembrane glycoprotein Gpnmb controls trafficking of cellular debris for degradation and is essential for tissue repair. *FASEB J* 24, 4767–4781 (2010).
122. Buza-Vidas, N. *et al.* Crucial role of FLT3 ligand in immune reconstitution after bone marrow transplantation and high-dose chemotherapy. *Blood* 110, 424–432 (2007).
123. Williams, K. M. *et al.* FLT3 ligand regulates thymic precursor cells and hematopoietic stem cells through interactions with CXCR4 and the marrow niche. *Exp Hematol* 52, 40–49 (2017).
124. Wagner, W. *et al.* Aging and Replicative Senescence Have Related Effects on Human Stem and Progenitor Cells. *PLoS ONE* 4, e5846 (2009).
125. Vaughan, S. & Jat, P. S. Deciphering the role of Nuclear Factor-κB in cellular senescence. *Aging* 3, 913–919 (2011).
126. Ferbeyre, G. Aberrant signaling and senescence associated protein degradation. *Experimental Gerontology* 107, 50–54 (2018).
127. Chou, C.-H. *et al.* Synovial cell cross-talk with cartilage plays a major role in the pathogenesis of osteoarthritis. *Sci Rep* 10, 10868 (2020).
128. Holzmuller, P., Nirdé, P., Vezilier, F. & Chuchana, P. The transcriptomic analytical level determines the human monocyte-derived macrophage response toward either the infectious agent or the host. *Infect Genet Evol* 45, 426–433 (2016).

Figures

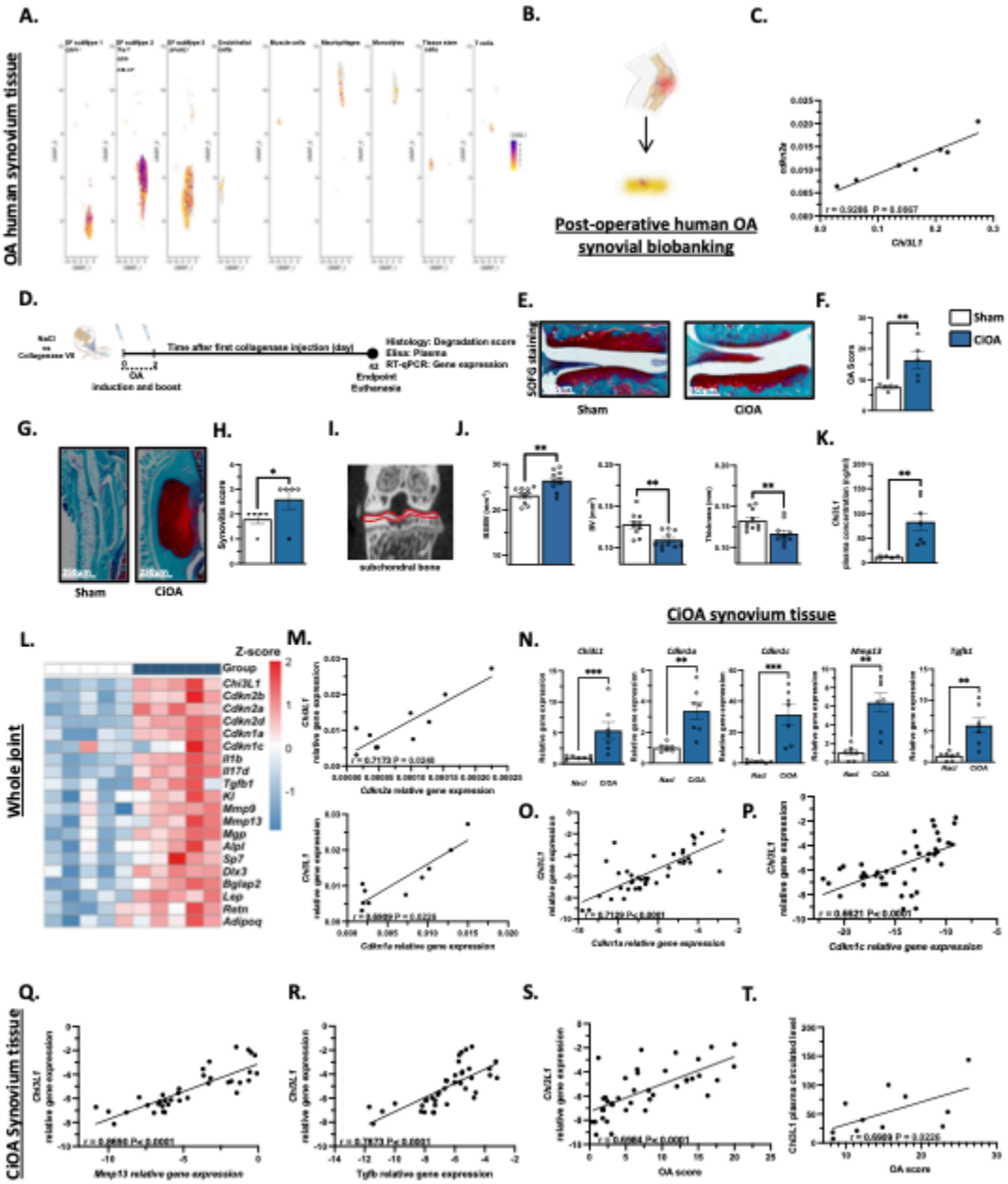

Fig. 1. **Chi3L1 corrrelates with senescence in OA synovium tissue and increased across different joint compartment in OA murin preclinical model**

Figure 1

Chi3L1 correlates with senescence in OA synovium tissue and increased across different joint compartment in OA murine preclinical model (A) UMAP visualization showing the differential expression of Chi3L1 across the human osteoarthritic synovium tissue subpopulation **(B)** Schematic of the postoperative knee synovial tissue biobanking **(C)** Scatter plot with a linear regression line showing the correlation between *CHI3L1* and *CDKN2A*mRNA expression in human osteoarthritic synovium tissue. Each dot represents one individual (n=7) **(D)** Schematic of the OA experimental design with timeline showing intra-articular injection of colVII (1U) vs NaCl (Sham), sacrifice at day 42 and subsequent

analyses **(E-F)** Representative histological image of joint cartilage sections assessed by SOFG staining and its corresponding OA score. Scale bar 250µm, each dot represents one mouse (n=5 per group) **(G-H)** Representative histological image of synovium sections assessed by SOFG and its corresponding synovitis score. Scale bar 250µm, each dot represents one mouse (n=5 per group**) (I-J)** Representative image of subchondral bone architecture and quantification of structural parameters: bone volume, bone surface/bone volume (BS/BV) and thickness. Each dot represents one individual (n=5 per group) **(K)** Relative quantification of Chi3L1 systemic level in CiOA vs Sham mice by Elisa. Each dot represents one mouse (n=5-7 per group) **(L)** Heatmap of gene expression (Z score) of selected genes expression in whole joint tissue. Each dot represents one mouse (n=5 per group) **(M)** Scatter plot with linear regression line showing the correlation between *Chi3L1* and both *Cdkn2a Cdkn1a* mRNA relative expressions in the whole joint. Each dot represents one mouse (n=10) **(N)** Relative quantification of selected genes level (*Chi3L1, Cdkn1a, Cdkn1c, Mmp13 and Tfgb1*) in synovial tissue. Each dot represents one mouse (n=7 per group) **(O-R)** Scatter plot with linear regression line showing the correlation between *Chi3L1* and *Cdkn1c, Mmp13, Cdkn1a, Tgfb1* mRNA relative expression in the synovial tissue. Each dot represents one mouse (n=40) **(S)** Scatter plot with linear regression line showing the correlation between *Chi3L1* mRNA expression in synovial tissue and OA grade. each dot represents one mouse (n=39) **(T)** Scatter plot linear regression line showing the correlation between Chi3L1's plasma level and OA grade of the same mice. (n=10)**.** Data are expressed as means ± SEM where applicable. *p < 0,05, **p < 0,01, ***p < 0,001. Statistical significance was assessed using Pearson's correlation analysis for (C) (M) (O) (R) (S), an unpaired two-tailed Mann-Whitney for (F) (H) (J) (K) (N) and multiple two-tailed corrected unpaired comparison t-tests for (L).

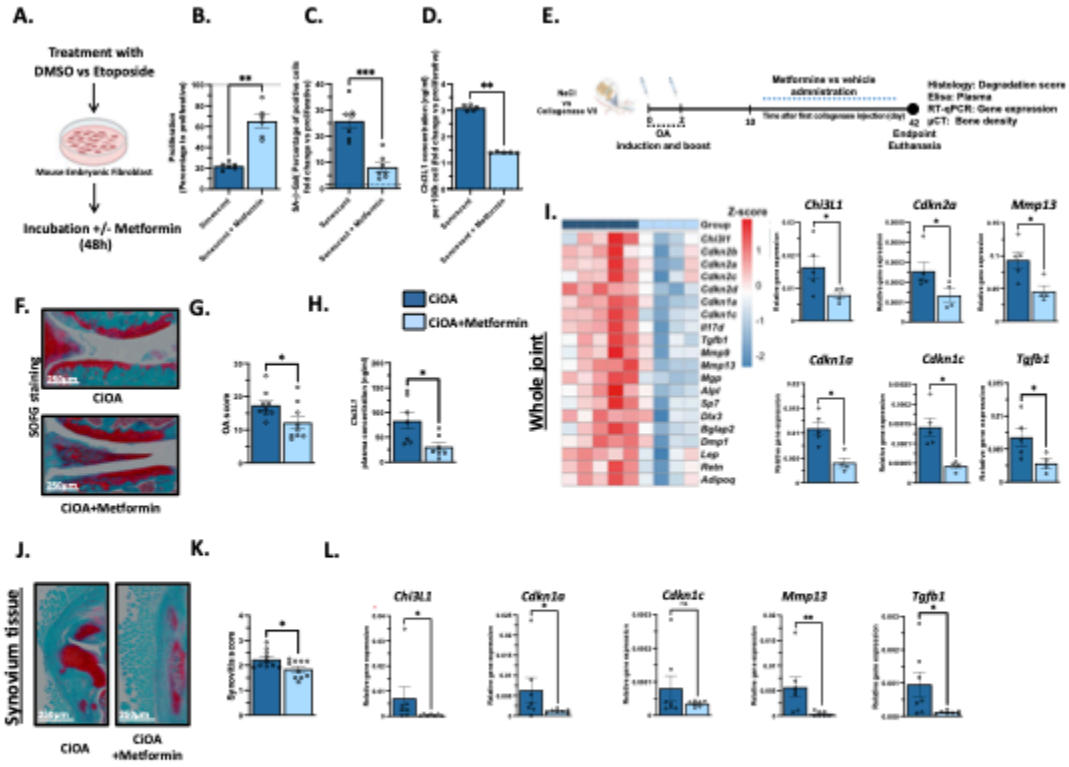

Fig. 2. **CHI3L1 production is increased in etoposide-induced senescent fibroblasts and decreases during metformin treatment in vitro and in experimental OA**

Figure 2

CHI3L1 production is increased in etoposide-induced senescent fibroblasts and decreases during metformin treatment in vitro and in experimental OA (A) Schematic showing MEF treatment with etoposide (20µM) vs DMSO than incubated with metformin (3mM) for seven days **(B-C)** Quantification of cells proliferation and SA-β-gal staining positive of proliferative MEF (DMSO) versus senescent (Etoposide) and senescent supplemented with metformin. Each dot represents an independent biological replicate (n=9 per group**) (D)** Relative quantification of Chi3L1 secreted level at day 7 by Elisa. Each dot represents an independent biological replicate (n=5 per group) **(E)** Schematic of the OA experimental design with timeline showing intra-articular injection of colVII (1U) vs NaCl (Sham) at day 0 and 2, metformin supplementation (from day10 till sacrifice), sacrifice at day 42 and subsequent analyses **(F-G)** Representative histological image of joint cartilage sections assessed by SOFG staining and its corresponding OA score. Scale bar 250µm, each dot represents one mouse (n=9 per group) **(H)** Relative quantification of Chi3L1 plasma level in CiOA and CiOA-metfromin mice by Elisa. Each dot represents one mouse (n=7 per group) **(I)** Relative quantification of selected genes expression in whole joint tissue. Each dot represents one mouse (n=4-5 per group) **(J-K)** Representative histological image of synovial tissue sections assessed by SOFG staining and its corresponding synovitis score. Scale bar 250µm, each dot represents one mouse (n=10 per group) **(L)** Relative quantification of selected genes level (*Chi3L1, Cdkn1a, Cdkn1c, Mmp13 and Tfgb1*) in synovial tissue. Each dot represents one mouse

(n=7 per group). Data are expressed as means ± SEM. *p < 0,05, **p < 0,01, ***p < 0,001. Unpaired two-tailed Man-Whitney test for (B) (C) (D) (L), unpaired two-tailed Student's t-test for (G) (H) (K), and multiple two-tailed corrected unpaired comparison t-test for (I).

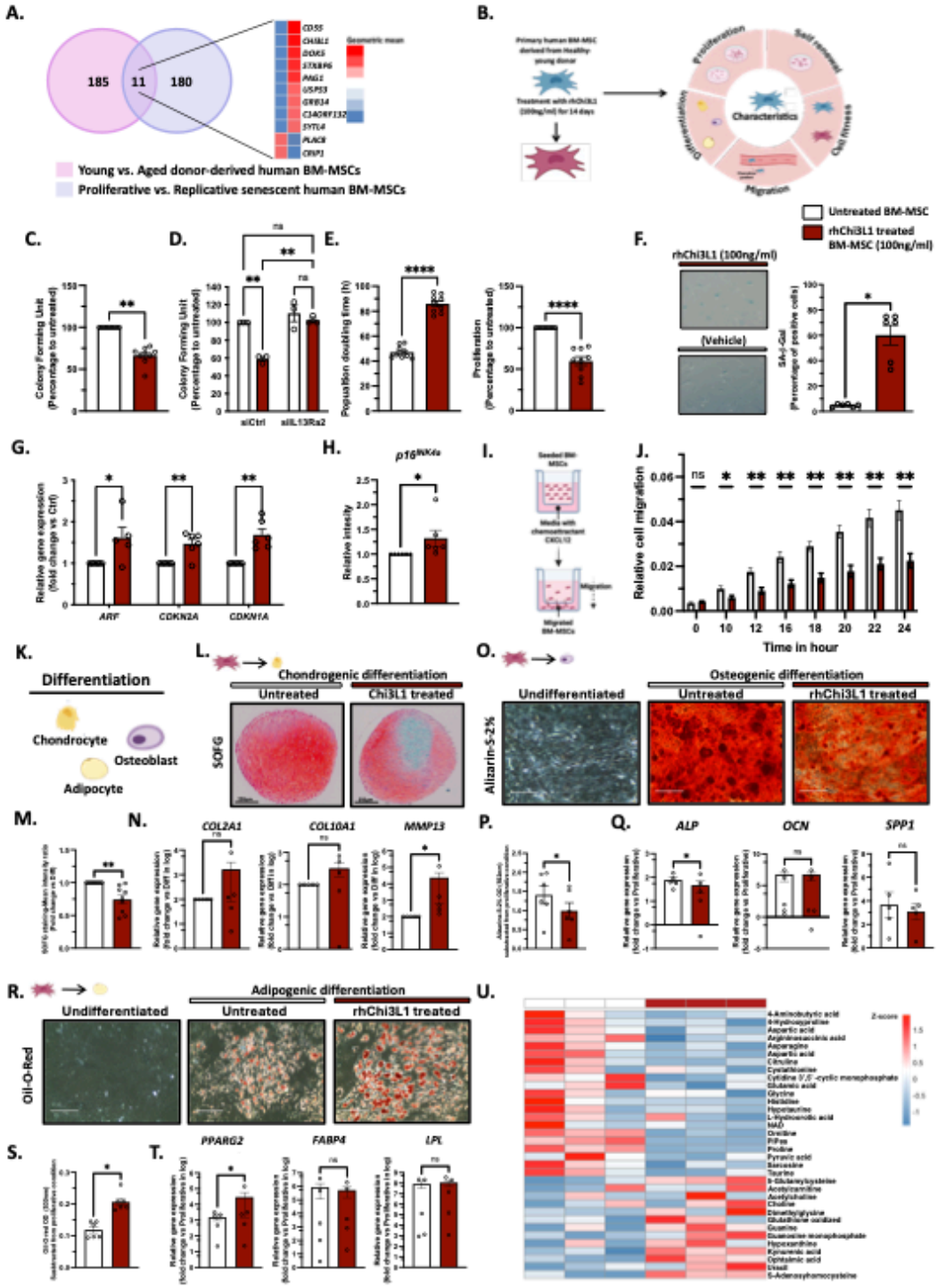

Fig. 3. **rhChi3L1 drives BM-MSCs stemness and metabolomic reprogramming toward a senescence-like phenotype**

Figure 3

rhChi3L1 drives BM-MSCs stemness and metabolomic reprogramming toward a senescence-like phenotype (A) Venn Diagram presenting the overlap of RNA-seq DEGs between senescent and aged BM-MSCs **(B)** Experimental design illustrating primary healthy young human BM-MSC cultures in the absence or chronic presence of rhChi3L1 (100ng/ml) for fourteen days **(C)** Relative quantification of the colony forming unit assay rate of untreated versus rhChi3L1 treated BM-MSC. Each dot represents an independent biological replicate (n=9 per group) **(D)** Relative quantification of the colony forming unit assay rate of siCtrl versus siIL13RA2 transfected BM-MSCs untreated versus rhCHI3L1 treated. Each dot represents an independent biological replicate (n=3 per group) **(E)** Relative quantification of the population doubling time and proliferation rate of untreated versus rhChi3L1 treated BM-MSC. Each dot represents an independent biological replicate (n=9 per group) **(F)** Representative image and quantification of SA-β-gal positive staining of untreated versus rhChi3L1 pretreated BM-MSCs. Scale bar 200µm each dot represents an independent biological replicate (n=6 per group) **(G)** Relative quantification of *ARF*, *CDKN2A* and *CDKN1A* mRNA level in untreated versus rhChi3L1 pretreated BM-MSC. Each dot represents an independent biological replicate (n=6 per group) **(H)** Relative quantification of $p16^{INK4a}$ protein level in untreated versus rhChi3L1 pretreated BM-MSC. Each dot represents an independent biological replicate (n=6 per group) **(I)** Schematic illustrating MSC migratory potential under CXCL12-mediated chemotaxis **(J)** Relative quantification of untreated or rhChi3L1 pre-treated BM-MSCs migrated number from 0 till 24hours post CXCl12 stimulation. Each dot represents an individual technical replicate from four independent biological replicates (n=4 independent biological replicates; three technical replicates per biological replicate). **(J)** Schematic illustrating BM-MSC trilineage differentiation ability **(K)** Representative image of chondrogenic differentiation of BM-MSCs treated or not with rhChi3L1 assessed by SOFG staining. Scale bar 250µm **(M)** Staining intensity quantification (RBG method) (Each dot represents an individual technical replicate from three independent biological replicates (n=3 independent biological replicates; three technical replicates per biological replicate) **(N)** Relative quantification of *COL2A1*, *COL10A1*, *MMP13* mRNA expression. Each dot represents an independent biological replicate (n=5 per group). **(O)** Representative image of osteoblastogenic differentiation of BM-MSCs treated or not with rhChi3L1 assessed by Alizarin-S-2%, scale bar 200µm **(P)** OD quantification (562nm). Each dot represents an independent biological replicate (n=6 per group) **(Q)** Relative quantification of *ALP*, *OCN*, *OPN* mRNA expression. Each dot represents an independent biological replicate (n=6 per group) **(R)** Representative image of adipogenic differentiation of BM-MSCs treated or not with rhChi3L1 assessed by Oil Red O Staining, scale bar 200µm **(S)** OD quantification (530nm). Each dot represents an independent biological replicate (n=6 per group). **(T)** Relative quantification *of PPARG2, FBP4, LPL* mRNA expression. Each dot represents an independent biological replicate (n=6 per group) **(U)** Heatmap of metabolites peak quantification (Z score) showing the metabolomic profiling of untreated vs rhChi3L1 pretreated BM-MSCs metabolites consistently upregulated or downregulated upon rhCHI3L1 treatment. Each dot represents an independent biological replicate (n=3 per group). Data are expressed as means ± SEM. *p < 0,05, **p < 0,01, ***p a< 0,001 Paired two-tailed Wilcoxon signed-rank test for (C) (E), (F) (H) (J) (M) (P) (S), corrected 2way ANOVA for (D), paired one-tailed Wilcoxon signed-rank test for (N) (Q) (T) and multiple two-tailed corrected t tests comparison for (G).

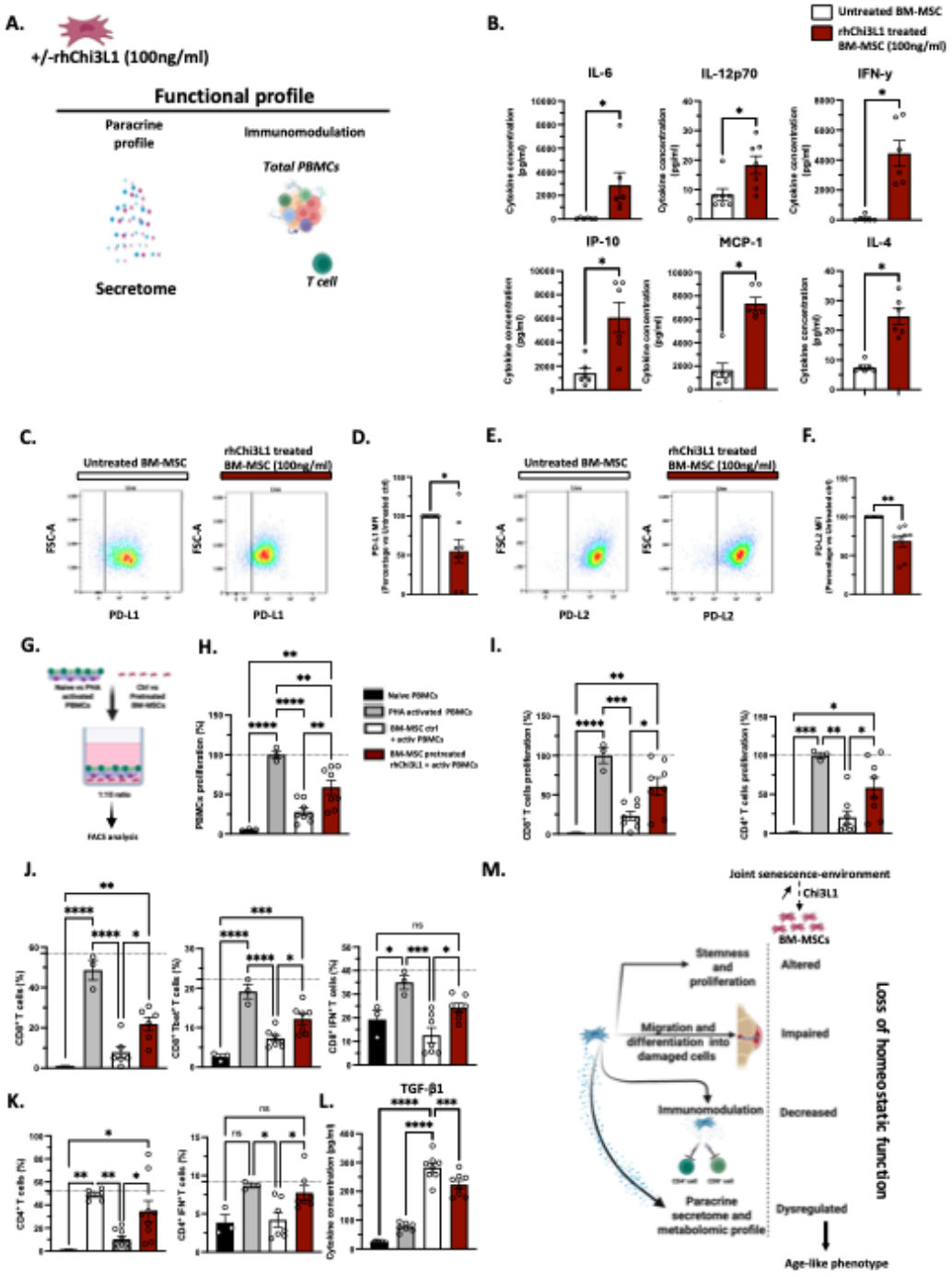

Fig. 4. **Chi3L1 impairs BM-MSCs exogeneous functional outputs and induces a pro-inflammatory state**

Figure 4

Chi3L1 impairs BM-MSCs exogeneous functional outputs and induces a pro-inflammatory state (A). Schematic illustrating BM-MSC functional output studied after rhChi3L1 (100ng/ml) or vehicle (PBS) pre-treatment for fourteen days **(B)** Flow cytometric quantification of paracrine factors (IL-6, IL12-p70, IFN-γ, IP-10, MCP-1, IL-4) released by untreated vs rhChi3L1-pretreated-BM-MSCs. Each dot represents an independent biological replicate (n=6 per group) **(C-F)** Representative Flow cytometry dot plots and

quantification of median fluorescence intensity in untreated vs rhChi3L1 pretreated BM-MSCs. Each dot represents an independent biological replicate (n=8 per group) **(G)** Schematic of MSC-PBMCs co-culture immunosuppression assay (1:10 ratio BM-MSC:PBMCs) with untreated vs rhChi3L1 pretreated, naive or activated PBMCs and BM-MSCs free control **(H)** Flow cytometric quantification of total PBMCs proliferation. Each dot represents an independent biological replicate (n=3-8 per group) **(I)** Flow cytometric quantification of $CD8^+$ and $CD4^+$ cells proliferation. Each dot represents an independent biological replicate (n=3-8 per group**) (J)** Flow cytometric quantification of $CD8^+$ and related subpopulation frequencies. Each dot represents an independent biological replicate. (n=3-7 per group) **(K)** Flow cytometric quantification of $CD4^+$ and related subpopulation frequencies. Each dot represents an independent biological replicate (n=3-8 per group) **(L)** Flow cytometric quantification of free TGF-β1 at the end of the immunosuppressive co-culture assay. Each dot represents an independent biological replicate (n=8 per group) **(M)** Schematic recapitulating effect of rhChi3L1 treatment on BM-MSCs potencies. Data are expressed as means ± SEM. *p < 0,05, **p < 0,01, ***p < 0,001. Paired two-tailed Wilcoxon signed-rank test for (B) (D) (F) and two-tailed corrected one-way ANOVA for (H) (I) (J) (K) (L).

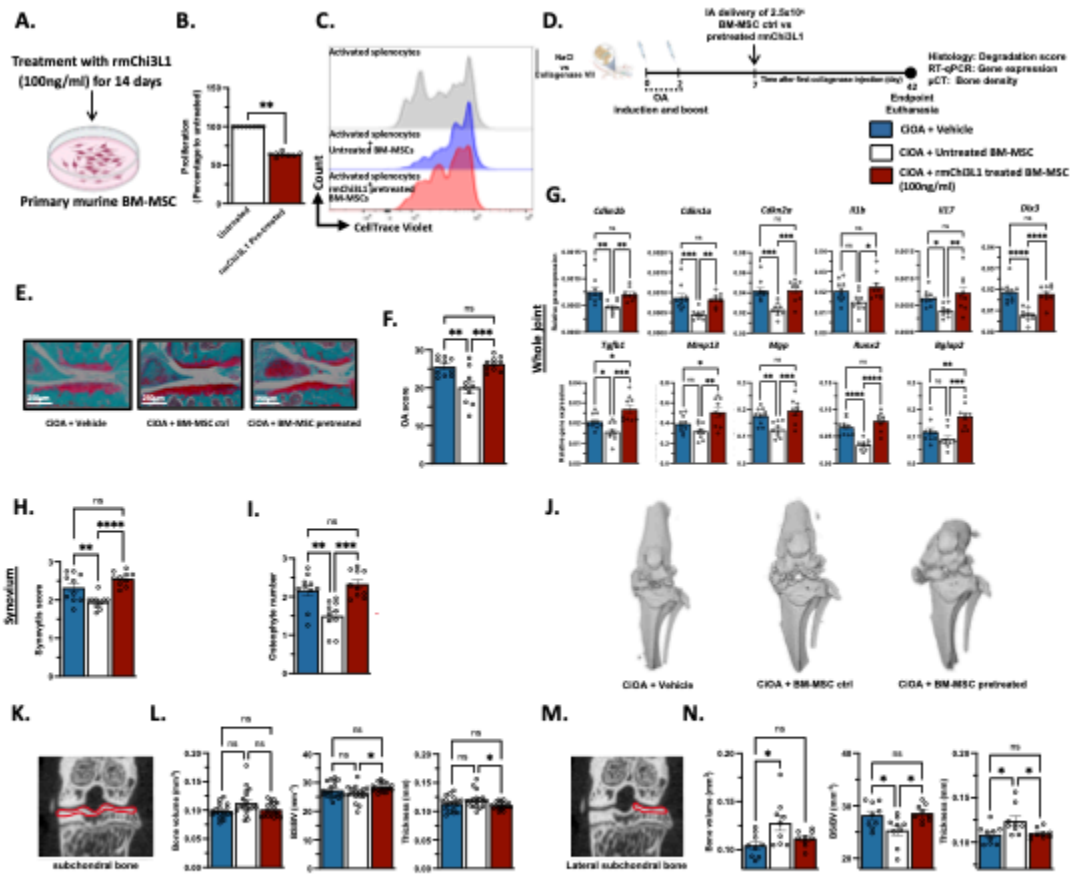

Fig. 5. **Chi3L1 pretreated BM-MSCs showed loss of homeostatic function in OA murine preclinical model following their intra-articular delivery**

Figure 5

Chi3L1 pretreated BM-MSCs showed loss of homeostatic function in OA murine preclinical model following their intra-articular delivery (A) Schematic illustrating BM-MSC treatment with rmChi3L1 (100ng/ml) vs vehicle for fourteen days **(B)** Relative quantification of the proliferation rate of untreated versus rmChi3L1 pretreated BM-MSC. Each dot represents an independent biological replicate (n=8 per group) **(C)** Representative flow cytometry histogram showing splenocytes proliferation assessed by CTV dilution in splenocytes cultured alone or co-cultured with untreated or rmChi3L1 pretreated BM-MSCs **(D)** Schematic of the OA experimental design with timeline showing intra-articular injection of colVII (1U) vs NaCl (Sham), vehicle control vs untreated BM-MSCs vs rmChi3L1-pretreated BM-MSC (at day 7), sacrifice at day 42 and subsequent analyses **(E-F)** Representative histological image of joint cartilage sections assessed by SOFG staining and its corresponding OA score. Scale bar 250µm, each dot represents a mouse (n=10 per group) **(G)** Relative quantification of selected gene expression level in whole joint tissue. Each dot represents a mouse (n=9-10 per group) **(H)** Quantification of synovitis score assessed on synovium sections. Each dot represents a mouse (n=10 per group**) (I)** Quantification of osteophyte score. Each dot represents a mouse (n=10 per group) **(J)** Representative 3D micro-CT reconstruction of hindlimb bone **(K-M)** Representative image of: subchondral bone **(L-N)** Quantification of joint subchondral bone microarchitectural parameters: bone volume, bone surface/bone volume (BS/BV) and thickness. Each dot represents a mouse (n=9 per group). Data are expressed as means ± SEM. *p < 0,05, **p < 0,01, ***p < 0,001. Paired two-tailed Wilcoxon signed-rank test for (B) two-tailed corrected ordinary one-way ANOVA for (F) (G) (H) (I) (L) (N).

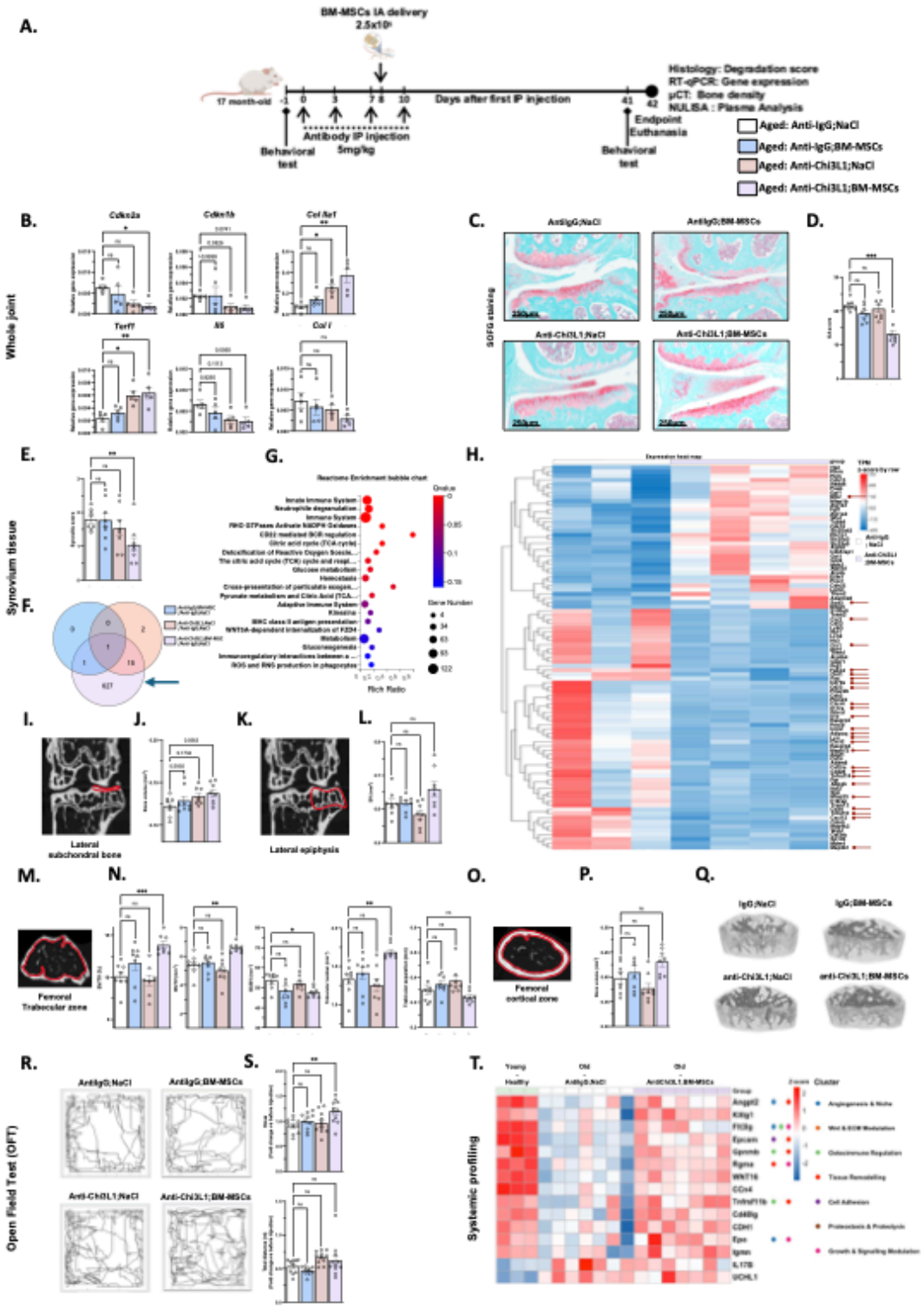

Fig. 6. **Chi3L1 neutralization and BM-MSCs co-injection promotes joint rejuvenation**

Figure 6

Chi3L1 neutralization and BM-MSCs co-injection promotes joint rejuvenation (A) Schematic of the experimental design with timeline showing repeated intra-peritoneal injection of IgG isotype or anti-Chi3L1 (5mg/Kg) injection at day 0-3-7-10, intra-articular injection of vehicle control (NaCl) vs healthy BM-MSCs ($2.5x10^5$ cell) at day 8, sacrifice at day 42 and subsequent analyses **(B)** Relative quantification of selected gene expression level in whole joint tissue. Each dot represents a mouse (n=5 per group) **(C-**

D) Representative histological image of joint cartilage sections assessed by SOFG staining and its corresponding OA score. Scale bar 250µm, aach dot represents a mouse (n=8-10 per group) **(E)** Synovitis score assessed on histological synovium sections on the experimental groups. Each dot represents a mouse (n=8 per group) **(F)** Venn Diagram presenting the overlap of RNA-seq DEGs in the synovium tissue **(G)** Reactome pathway enrichment analysis of DEGs in combination vs control **(H)** Heatmap of gene expression (TPM) for genes associated with reactome pathways. Each dot represents a mouse (n=3-4 per group) **(I-K)** Representative image of lateral: subchondral bone and epiphysis **(J-L)** Quantification of bone volume of lateral subchondral bone and lateral epiphysis. Each dot represents a mouse (n=8 per group) **(M)** Representative image of femoral trabecular zone **(N)** Quantification of femoral trabecular zone microarchitectural parameters: bone volume/tissue volume (BV/TV), bone surface/tissue surface (BS/TS), bone surface/bone volume (BS/BV), trabecular number and trabecular separation. Each dot represents a mouse (n=8 per group) **(O)** Representative image of femoral cortical zone **(P)** Quantification of femoral cortical zone bone volume. Each dot represents a mouse (n=8 per group) **(Q)** Representative 3D micro-CT reconstruction of femoral cortical and trabecular bone beneath the growth plate **(R)** Representative gait paths (T) Relative quantification and measurement of maximum speed and total distance attained by mice at the end point, as fold change to pre-injection values. Each dot represents a mouse (n=10-11 per group) **(T)** Heatmap (z score) presenting the relative quantification of circulating mediators by NULISA-based profiling. Each dot represents a mouse (n=3-7 per group). Data are expressed as means ± SEM. *p < 0,05, **p < 0,01, ***p < 0,001. Two-tailed corrected Kruksal-Wallis test for (B) (D) (E) (J) (L) (N) (P) (S) and 2way ANOVA for (T).

Supplementary Files

This is a list of supplementary files associated with this preprint. Click to download.

- Suppfig.docx